THE ASTROPHYSICAL JOURNAL, 441:307–333, 1995 March 1

THE DECELERATION POWERING OF SYNCHROTRON EMISSION FROM EJECTA COMPONENTS IN SUPERNOVA REMNANT CASSIOPEIA A

M. C. ANDERSON AND L. RUDNICK
Astronomy Department, University of Minnesota, Minneapolis, MN 55455
Received 1993 August 30; accepted 1994 September 15

ABSTRACT

The results of a multiple-epoch radio study of secular changes in the SNR Cassiopeia A are reported and used to construct a model for the dynamical evolution of diffuse and clumpy ejecta components in the remnant.

To quantify the current dynamical status of various ejecta components, the proper motions and brightness evolution of a sample of 304 compact radio features have been accurately determined from high-quality interferometric observations of the remnant at $\lambda = 6$ and 20 cm, spanning a total time baseline of 12 yr. A simple model of homologous expansion does not provide a good fit to the measured proper motions of the radio knots. We find that a single estimate of the ejecta expansion age is not appropriate, as the expansion derived from compact features varies azimuthally and radially in the remnant and differs for subsets of knots segregated by brightness. We verify that the bulk of the radio-emitting plasma in Cas A has indeed been significantly decelerated by the current epoch; bulk expansion ages of 2.5–4 times the actual age of the remnant are measured.

Based on these dynamical data, and information on the kinematics of the fast moving optical knots, we synthesize a model that directly relates the dynamics of ejecta components in Cas A to various radiative processes. This model is based on the premise that the emission from Cas A, at a variety of wavelengths, is deceleration-powered. If ejecta components are distributed over a range of internal densities, a sequential "turning-on" of components, in order of increasing density, should be observed. A model for the current emission distribution in Cas A, at radio, X-ray, and optical wavelengths, is outlined in terms of deceleration considerations.

Subject headings: ISM: individual (Cassiopeia A) — ISM: kinematics and dynamics — ISM: structure — supernova remnants — techniques: interferometric

1. INTRODUCTION

The standard interpretation of large-scale emission structures in the young supernova remnant (SNR) Cassiopeia A invokes deceleration as the major power source. The main radio ring is commonly associated with a region of high magnetic field strength, amplified through Rayleigh-Taylor instabilities occurring at the contact discontinuity between the ejecta and the shock-heated ISM which are triggered when the remnant enters its deceleration phase (Gull 1973a, b, 1975). The bulk of the X-ray–emitting material in Cas A is found in a clumpy shell of size and thickness similar to that of the bright radio ring. The soft X-ray flux from Cas A is most successfully modeled in terms of emission from a reverse shock interior to the contact discontinuity, driven back into the outflowing ejecta as the remnant begins to decelerate (McKee 1974). Evolutionary models predict that the reverse shock and contact discontinuity will not have separated much over the historical age inferred for Cas A (313 yr at the time of writing; Ashworth 1980), hence the spatial coincidence of the X-ray and radio rings. At the same time, this surface is populated by the fast-moving optical knots (FMKs; Reed et al. 1994, hereafter RHFW). These FMKs are moving at velocities ~ 5000 km s^{-1}, with some up to 8600 km s^{-1} (Fesen, Becker, & Goodrich 1988). If undecelerated, the positions and velocities of these knots are consistent with the age of the remnant.

The dynamics of this X-ray/radio/optical ring are therefore of great interest. However, proper motion studies of large-scale radio features have yielded conflicting results concerning the bulk expansion of the radio ring: Tuffs (1986) measures significant deceleration of bulk features in Cas A, while Green (1988) measures a bulk expansion rate more comparable to that of the undecelerated FMKs. Confirmation of the role of deceleration in powering SNR emission is further complicated in that the growth in synchrotron emissivity is expected, according to Gull's (1975) model, to occur over a very long timescale (hundreds of years).

Here, we confirm a relationship between deceleration and synchrotron brightness among *small-scale* radio emission features in Cas A, based on multiple-epoch, high-quality interferometric observations, spanning a total time baseline of 12 yr. Previous studies of the proper motions and radio brightness evolution of compact features in Cas A are reviewed in § 2 and an overview of our new study is provided in § 3. The results of these measurements are examined in § 4—in particular, we are interested in deriving expansion timescales for comparison with SNR evolutionary models, and in searching for possible correlations between dynamically important quantities. A measurement of the bulk expansion of Cas A is discussed in § 5 for comparison with the dynamics of small-scale structures, and in § 7 we propose a model in which deceleration provides the emission power for both large- and small-scale structures in the remnant. A comparison between this model and numerical cloud simulations is presented by Anderson et al. (1994, hereafter AJRTK). The dynamics established in this paper are used by Anderson & Rudnick (1995, hereafter AR) to address the question of relativistic particle acceleration in Cas A.

In keeping with previous discussions of radio and optical proper motions in Cas A, we will quantify deceleration in terms

of the "expansion timescale," $T = R/V_r$, where R is the projected radius of a given feature and V_r is its current radial proper motion, both measured with respect to the radio expansion center. Features with expansion timescales greater than the actual age of the remnant (~ 300 yr) have been decelerated from their initial ejection velocities. Models of SNR evolution typically use the "expansion parameter," x, where $R \propto t^x$, as a measure of deceleration; $x = 1$ indicates free expansion. The expansion parameter can be obtained from the expansion timescale if the true age of the remnant (t) is known: $x = t/T$.

2. PREVIOUS STUDIES OF SECULAR CHANGE IN CASSIOPEIA A

Previous efforts to measure secular changes in the radio-emitting material in Cas A have provided conflicting answers as to whether the radio emission exhibits an overall expansion and how the observed secular decrease in integrated flux density is distributed spatially across the remnant. These studies are summarized below and are compared with our results in § 3.

2.1. *Radio Proper Motions*

Bell (1977) studied secular changes in Cas A by comparing 5 GHz images at $\sim 7''$ resolution from epochs 1969 (Rosenberg 1970) and 1974 (Bell, Gull, & Kenderdine 1975), made with the Cambridge One-Mile and 5 km Telescopes, respectively. The motions of 34 bright knots were measured by shifting superposed images by eye to obtain optimal spatial correlation. Bell found considerable scatter in a plot of velocity versus distance from the optical expansion center, indicating a significant disordered component of motion comparable in magnitude to the ordered component. An error-weighted fit to all knots yielded an expansion age of 918 yr.

Contrary to the results of Bell (1977), Dickel & Greisen (1979), in a comparison of $7''$ resolution images at 2.7 GHz obtained with the NRAO three-element interferometer, found *no* evidence for ordered expansion among 83 radio features in Cas A. The differing results were attributed to possible confusion due to inadequate resolution and to differences in aperture coverage.

The 1974 observations used by Bell (1977) were compared by Tuffs (1986) at higher resolution ($2''$) to an epoch 1978 image at 5 GHz taken with the Cambridge 5 km Telescope. Tuffs measured the proper motions of 342 compact radio features using a least-squares minimization technique. The expansion center determined from a fit to all 324 knots was $\alpha(1950) = 23^h21^m10^s.2$, $\delta(1950) = +58°32'19''.7$, with 1 σ errors of $5''.5$ in right ascension and $4''.4$ in declination. An overall fit to proper motion as a function of radius yielded a net expansion age of 949^{+44}_{-41} yr, with some evidence that this age may shorten with radial distance from the remnant center. When the vector components of proper motion were considered separately, expansion ages of 1013^{+65}_{-57} yr in right ascension and 866^{+84}_{-48} yr in declination were obtained. The visual impression given by the distribution of proper motion vectors derived by Tuffs is one of overall expansion superposed with a significant random motion component. Tuffs found no significant difference between the motions of compact features and large-scale structures in the ring (see his Fig. 5).

Green (1988) points out that the compact radio knots used in the above studies comprise only a small fraction of the total radio-emitting mass (Tuffs [1986] estimates 19% resides in compact features), thus their motions may not be indicative of the bulk expansion of the remnant. Green measures the bulk expansion by looking for a contraction of features in the visibility plane (which is the Fourier transform of the sky brightness distribution), comparing data obtained with the Cambridge Low-Frequency Synthesis Telescope at 151 MHz in 1984 and 1986. For the most well-defined u-v features, contractions corresponding to an expansion age of ~ 400 yr were detected. This is more in keeping with the timescale defined by the expansion of the fast-moving optical knots (van den Bergh & Kamper 1983; RHFW) and thus, if accurate, would indicate an insignificant deceleration of the radio component. This finding has tremendous ramifications for the interpretation of different structures in the remnant; according to current models, without deceleration there can be neither a well-developed reverse shock nor significant Rayleigh-Taylor–related magnetic field amplification.

2.2. *Brightness Changes*

Bell (1977) examined brightness changes in Cas A by subtracting an epoch 1969 image at 5 GHz from a 1974 image. From this "difference map," the change in brightness of large-scale and slow-movng small-scale emission features can be deduced. Bell's difference map suggested that the north and northwestern and the southeastern parts of the remnant were brightening with time, while much of the central region was fading. Several compact features were found to have brightened considerably in this time interval, with only one knot showing a significant brightness decrease.

A difference map produced by Dickel & Greisen (1979) indicated a net decrease in brightness across the remnant of $\sim 1.7\%$ yr^{-1}, with the greatest decreases found in the southeast and the north. The western part of the remnant appeared to be fading less rapidly. Their data showed that most compact features were fading, with a mean brightness change for fading features of $-3.5\% \pm 1.5$ yr^{-1}. Brightening features showed a mean change of $+2.7\% \pm 2.5$ yr^{-1}. A mean $1/e$ lifetime of 48 yr was found for fading features.

Tuffs (1986) generated a difference map highlighting brightness changes occurring between epochs 1974 and 1978. The resultant map shows the western half of the remnant to be brightening, while the eastern half fades. This map suggests that the radio ring is fading at a rate of 1.32% yr^{-1}. Tuffs' data agree with those of Dickel & Greisen (1979) in concluding that most compact features are fading with time, although he obtains a mean decay rate of 1.57% yr^{-1} (Tuffs 1983).

3. NEW MULTIEPOCH STUDY OF SMALL-SCALE SECULAR CHANGE IN CASSIOPEIA A

In this section we discuss a new study of the temporal evolution of compact radio features in Cas A. Observational details are summarized in § 3.1—an outline of the method of measurement and a tabulation of results follow. Those uninterested in the technical details of this study should skip to § 4 for a discussion of the results.

3.1. *The Cassiopeia A Radio Image Archive*

The observations of Cas A discussed in the following are the result of an ongoing program to maintain a temporal archive of radio interferometric images of this unique remnant. As part of this effort, observations have been made with the Cambridge 5 km telescope and the Very Large Array (VLA[1]; Napier,

[1] The Very Large Array is a facility of the National Radio Astronomy Observatory, operated by Associated Universities, Inc., under contract with the National Science Foundation.

Thompson, & Ekers 1983) at ~2 yr intervals since 1978. Special care has been taken to maximize aperture coverage in order to sample the large range of spatial scales present in Cas A. Thus, these images represent some of the most detailed radio astronomical images yet produced. We have added to the archive a 1990 epoch pair of observations at $\lambda = 6$ and 20 cm (C- and L-bands). Observational details of this archive are summarized in Tables 1 and 2. The typical hour angle coverage for each of the VLA observing sessions was on the order of 9 hr.

Due to the spatial complexity of the remnant, data at each observing band have been obtained in all four standard VLA configurations at each epoch and combined in the final image synthesis (the A-configuration data at C-band have been excluded in most cases to match the resolution of the L-band data). To further improve aperture coverage, a technique known as "bandwidth synthesis" was used, whereby data are collected at several frequencies in a narrow band around the nominal frequency. The utilization of bandwidth synthesis does not greatly affect the results discussed in this paper, but must be considered in accompanying papers on polarization (Anderson, Keohane, & Rudnick 1995, hereafter AKR) and spectral index (AR).

Calibration and image reconstruction procedures used for all epochs follow closely after those applied to the epoch 1987 data, as outlined by Anderson et al. (1991). Dirty images at each band and epoch have been deconvolved with the AIPS Maximum Entropy routine VTESS. Although target zero-spacing flux densities were not specified, VTESS was typically able to reconstruct 95% of the total expected flux at L-band (given by the Baars' flux scale; Baars et al. 1977, as modified in the 1990 VLA Calibrator Manual) and 85% at C-band. All images have been corrected for primary beam attenuation and have been convolved with a circular Gaussian function of diameter 1".3 to fix the resolution. A normalization method, described below, has been developed to compensate for minor differences in absolute flux calibration and aperture coverage between epochs.

The study of the evolution of compact radio structures in Cas A presented in this work derives from the series of six $\lambda = 6$ cm images in the archive, spanning a total time baseline of 12 yr. Measurements of the bulk expansion of the large-scale radio ring (§ 5) have been conducted at $\lambda = 20$ cm, where the sampling of the inner portion of the aperture plane is more complete.

3.1.1. *Anatomy of Cassiopeia A*

The epoch 1987 λ 20 cm image from the Cas A radio archive is shown in Figure 1 (Plate 6). This gray-scale demonstrates the quality of imagery contained in this archive; it also reveals

TABLE 1

SUMMARY OF $\lambda = 6$ CENTIMETER CASSIOPEIA A OBSERVATIONS

Instrument	Array	Date	Frequencies (MHz)	Bandwidth (MHz)	Integration Time (s)
			Epoch 1978		
5 km[a]		1978.9	4995	10	60
			Epoch 1982		
5 km[a]		1982.4	4995	10	60
			Epoch 1983		
VLA[a,b,c]	B	1984.00	4640, 4970	6.25	10
	C	1983.09	4885	50.0	30
	D	1982.95	4885	50.0	30
			Epoch 1985		
VLA[a,c,d]	B	1985.29	4640, 4970	6.25	10
	C	1985.72	4832, 4902	12.5	30
	D	1986.04	4816, 4866	12.5	30
			Epoch 1987		
VLA[b,c,e,f]	B	1987.88	4640, 4970	6.25	10
	C	1988.19	4816, 4866	12.5	30
	C	1988.23	4823, 4873	12.5	30
	D	1987.35	4835, 4885	50.0	30
			Epoch 1990		
VLA[e,f,g]	B	1990.71	4613, 4943	6.25	10
	C	1990.90	4816, 4823, 4866, 4873	12.5	30
	D	1991.25	4835, 4885	50.0	30

[a] R. J. Tuffs.
[b] S. F. Gull.
[c] R. A. Perley.
[d] P. H. Angerhofer.
[e] R. Braun.
[f] L. Rudnick.
[g] M. C. Anderson.

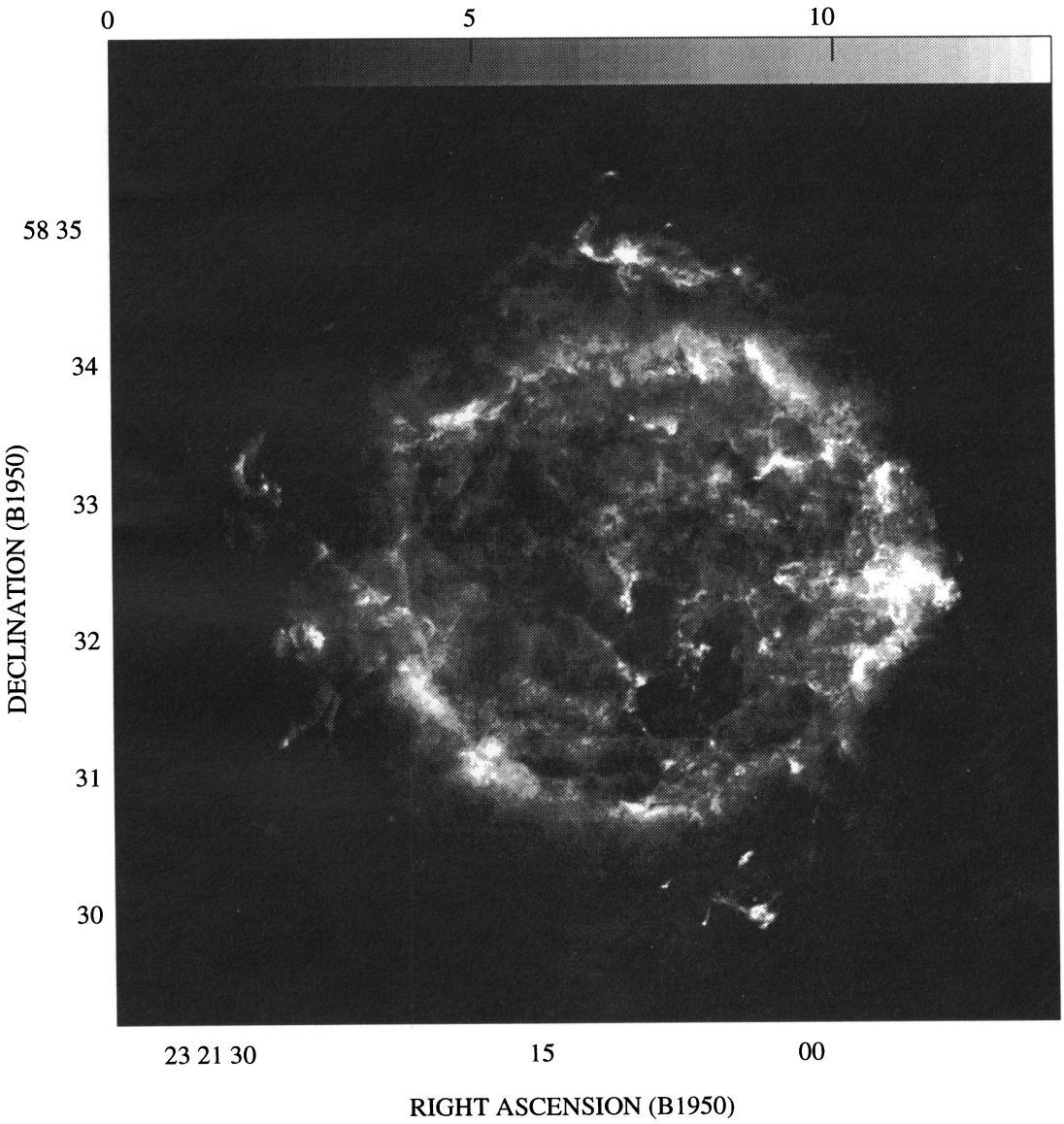

FIG. 1.—Total intensity image of Cas A at $\lambda = 20$ cm from epoch 1987 (1".3 resolution). Gray-scale is in units of mJy beam^{-1}.

ANDERSON & RUDNICK (see 441, 309)

TABLE 2

SUMMARY OF $\lambda = 20$ CENTIMETER CASSIOPEIA A OBSERVATIONS

Instrument	Array	Date	Frequencies (MHz)	Bandwidth (MHz)	Integration Time (s)
			Epoch 1985		
VLA[a,b,c]	A	1985.16	1381, 1456, 1536, 1626	3.125	10
	B	1985.29	1381, 1626	6.25	10
	C	1985.72	1482, 1512	12.50	30
	D	1986.04	1446, 1496	12.50	30
			Epoch 1987		
VLA[c,d,e,f]	A	1987.58	1381, 1456	3.125	10
	A	1987.62	1536, 1626	3.125	10
	B	1987.88	1381, 1635	6.25	10
	C	1988.19	1446, 1496	12.5	30
	C	1988.23	1446, 1496	12.5	30
	D	1987.35	1465, 1515	50.0	30
			Epoch 1990		
VLA[e,f,g]	A	1990.45	1362, 1441, 1512, 1612	3.125	10
	B	1990.71	1363, 1613	6.25	10
	C	1990.90	1446, 1496	12.5	30
	D	1991.25	1465, 1515	50.0	30

[a] R. J. Tuffs.
[b] P. H. Angerhofer.
[c] R. A. Perley.
[d] S. F. Gull.
[e] R. Braun.
[f] L. Rudnick.
[g] M. C. Anderson.

the structural complexity of this remarkable radio source. We introduce here, for future reference, a few of the most notable structures in the remnant.

The radio morphology of SNR Cas A is dominated by a bright, clumpy *ring* of radius $\sim 100''$ (1.7 pc at a distance of 2.9 kpc). The ring has a bright component $\sim 10''$ wide, which sits on top of a broader component of $\sim 30''$ width. As was stated above, this ring is typically associated with a zone of amplified magnetic field, generated at the contact discontinuity during deceleration. The X-ray ring (Fabian et al. 1980) and shell of optical knots (RHFW) are found at the same radius.

A fainter *plateau* of emission, offset somewhat to the east with respect to the radio ring, is seen out to a radius of $\sim 140''$. This plateau may correspond to a region of lower surface brightness between the outer blast wave and the contact discontinuity, illuminated by energetic electrons which have diffused from one or both surfaces (see Braun 1987 for an alternative explanation).

Braun, Gull, & Perley (1987, hereafter BGP) have identified a group of 11 compact radio structures in Cas A resembling *bow shocks*, both morphologically and polarimetrically, The most prominent of these are the paraboloidal structures seen protruding from the northern and southern edges of the diffuse plateau emission in Figure 1. BGP suggest that these features are associated with clumps of moderately fast-moving ejecta which have recently penetrated the decelerated radio shell—in this case, the emission we see in these structures emanates not from the clumps themselves, but from background material compressed by the bow-shocks preceding them.

To the east-northeast, the bright radio shell appears to be ruptured. The plateau at this position angle is extended, and contains several discrete knots far from the shell center. This protrusion, often called the *jet* or *flare*, is delineated in optical imagery by a population of exceptionally fast FMKs, with proper motions of 0.″6–0.″7 yr^{-1} (Kamper & van den Bergh 1976) and Doppler velocities of up to 8600 km s^{-1} (Fesen, Becker, & Goodrich 1988). We will see that the jet region exhibits distinctive kinematic properties at radio wavelengths as well.

3.2. *Selection of Compact Radio Features*

The sample of radio knots used in the present study were selected, in part, from the compendium of 342 discrete features compiled by Tuffs (1986). Features were retained from this list if (1) they were clearly visible in each of the six $\lambda = 6$ cm images, (2) they did not drastically change shape over the 12 yr time period encompassed by the archive, and (3) they were not in highly confused regions, and thus could be isolated from other emission structures. To include knots that may have been faint in 1978 but brighter at later epochs, a contour plot of the 1987 image was constructured and all local maxima therein were examined and added to our sample if not already present. These criteria defined a final sample of 304 knots. The positions of these knots are displayed in Figure 2 (Plates 7–8) and are documented, along with other measured quantities, in Table 3.

3.3. *Image Normalization*

It is essential to this effort that we be able to isolate changes in our data that are real from those that are instrumentally induced. Our greatest concerns in this regard lie with differences between epochs in calibration and aperture coverage. Clearly the adoption of different flux standards will impose a multiplicative gain factor between epochs. Varying the aper-

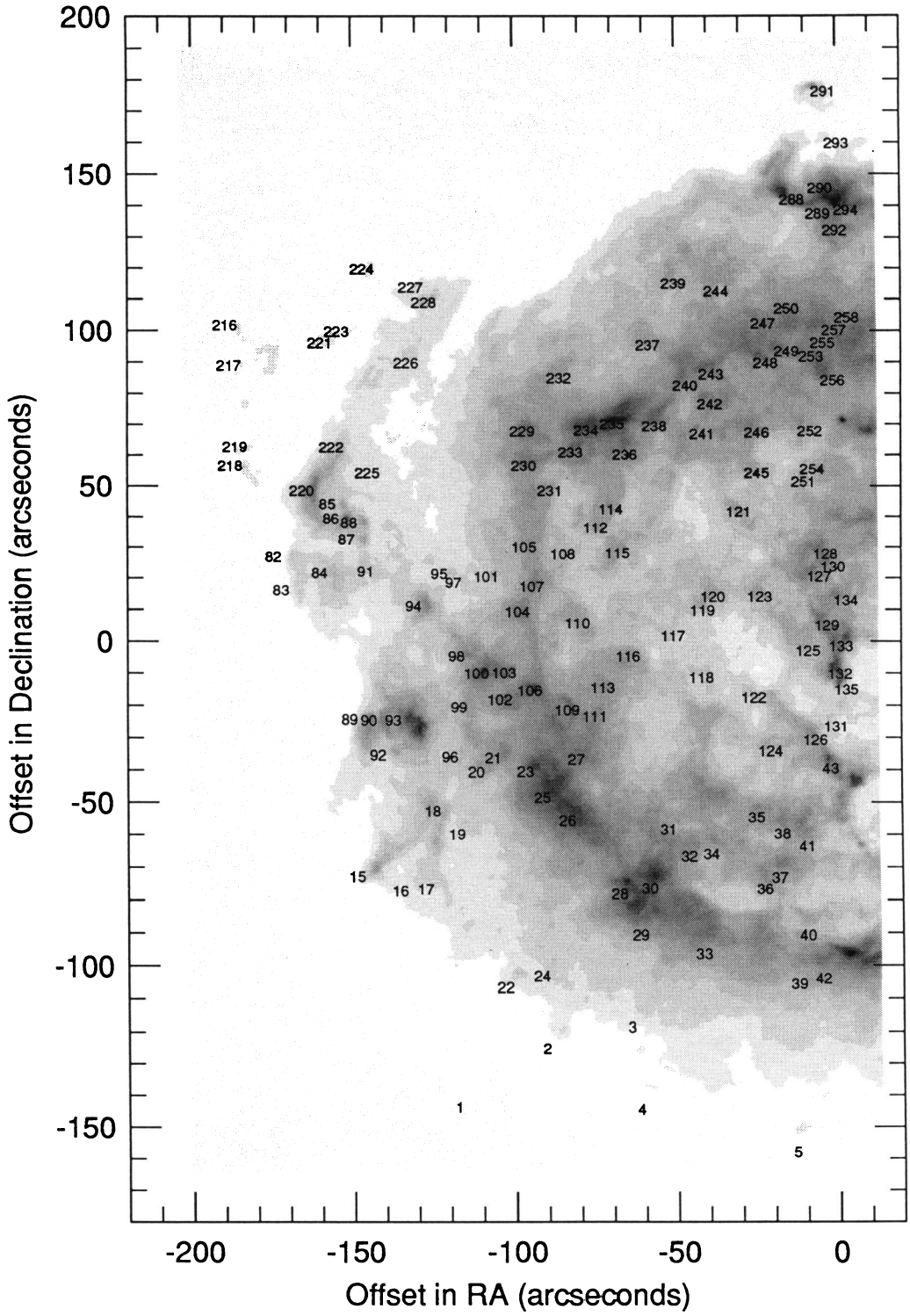

FIG. 2*a*

FIG. 2.—Positions of the radio knots studied in this work. Designation labels for knots (*a*) in the eastern hemisphere and (*b*) in the western hemisphere are overlaid on a full resolution gray-scale image of Cas A constructed from the epoch 1987 $\lambda = 6$ cm observations.

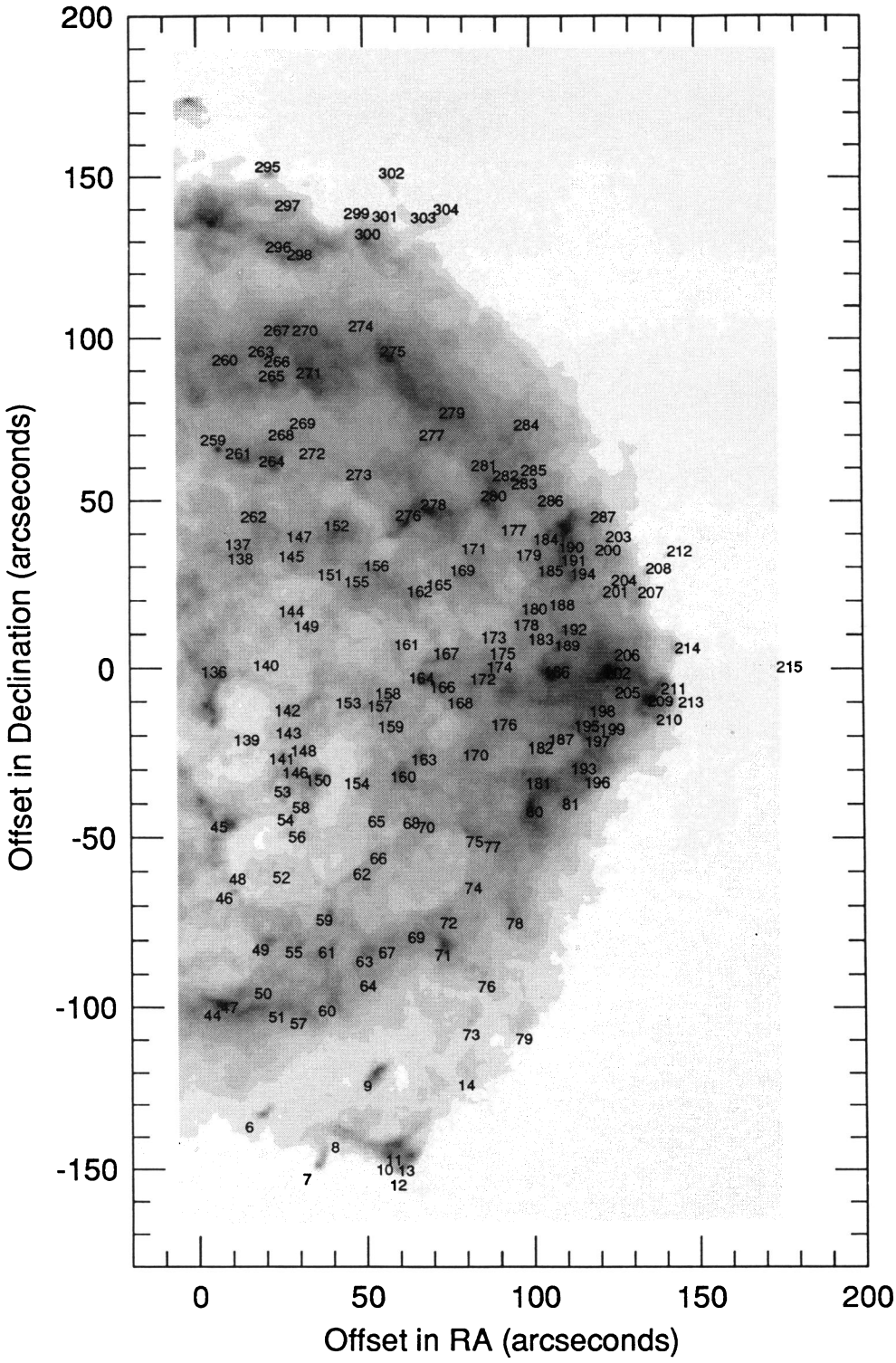

FIG. 2*b*

ANDERSON & RUDNICK (see 441, 310)

TABLE 3

RESULTS OF MULTI-EPOCH FITS

Knot	Knot_T	x	y	Box_{x1}	Box_{y1}	Box_{x2}	Box_{y2}	V_x	δV_x	V_y	δV_y	B	$\frac{\Delta B}{B}$	$\delta\frac{\Delta B}{B}$	#
1	9	-106.8	-135.7	-119.0	-141.8	-103.4	-129.8	-0.326	0.044	-0.328	0.034	2.1	0.038	0.029	5
2	15	-79.8	-117.2	-86.2	-122.2	-75.0	-109.4	-0.100	0.019	-0.239	0.022	6.9	0.080	0.010	5
3	20	-53.4	-110.6	-57.8	-116.6	-49.8	-108.2	-0.108	0.042	-0.406	0.044	3.7	0.012	0.025	5
4	6	-50.5	-136.4	-58.2	-142.2	-45.0	-131.4	-0.261	0.045	-0.243	0.032	2.5	0.021	0.025	5
5	1	-2.6	-149.9	-9.8	-156.6	4.6	-147.0	0.092	0.055	-0.210	0.029	3.6	0.026	0.024	4
6	12	25.5	-128.9	20.6	-132.6	31.0	-123.4	0.049	0.013	-0.130	0.009	36.5	0.090	0.005	5
7	3	42.7	-144.8	37.4	-153.0	45.0	-142.6	-0.051	0.009	-0.111	0.011	29.0	-0.147	0.010	6
8	7	51.1	-135.1	44.6	-139.4	55.0	-129.8	-0.022	0.022	-0.159	0.014	14.9	0.026	0.007	5
9	14	61.0	-115.8	54.6	-123.4	67.8	-111.0	0.077	0.011	-0.026	0.011	62.2	0.023	0.004	6
10	4	64.6	-141.8	60.2	-145.4	67.4	-139.4	0.001	0.019	-0.066	0.017	37.0	0.038	0.013	4
11		67.4	-139.0	64.6	-141.8	71.4	-134.2	0.063	0.027	-0.026	0.016	44.5	0.072	0.012	5
12		68.6	-146.6	64.6	-149.8	72.2	-144.2	0.084	0.015	-0.132	0.016	25.6	0.009	0.009	5
13		71.0	-142.2	67.8	-145.0	74.6	-139.4	0.100	0.017	-0.132	0.014	41.7	0.061	0.006	6
14	17	89.3	-115.5	84.6	-122.2	95.8	-108.6	0.075	0.018	-0.155	0.027	5.3	0.016	0.009	6
15	61	-139.2	-64.9	-143.4	-69.4	-136.2	-61.0	-0.226	0.013	-0.178	0.016	24.6	0.033	0.007	6
16	59	-125.9	-69.2	-129.4	-73.0	-122.2	-65.8	-0.171	0.041	-0.154	0.046	2.9	0.013	0.020	5
17	49	-118.0	-68.6	-121.4	-73.0	-114.6	-65.8	-0.200	0.032	-0.201	0.045	3.4	0.086	0.022	4
18	78	-115.8	-44.6	-118.2	-49.4	-111.8	-39.8	-0.141	0.009	-0.144	0.017	7.2	0.031	0.008	6
19	75	-108.2	-51.8	-112.6	-56.6	-103.8	-47.4	-0.128	0.025	-0.161	0.028	2.9	0.012	0.020	6
20	97	-102.2	-32.5	-106.2	-36.2	-99.0	-29.4	-0.134	0.018	-0.069	0.014	7.7	-0.024	0.011	6
21	101	-97.0	-28.2	-101.0	-33.0	-93.4	-23.8	-0.165	0.012	-0.047	0.017	10.3	0.012	0.007	6
22		-93.6	-98.6	-98.2	-104.2	-89.0	-95.0	-0.065	0.012	-0.129	0.012	9.0	0.063	0.007	6
23		-87.1	-32.4	-92.2	-36.6	-83.4	-28.2	-0.140	0.008	-0.084	0.007	21.7	-0.017	0.004	6
24	31	-82.4	-95.2	-86.2	-99.8	-79.4	-92.2	-0.136	0.026	-0.211	0.029	3.2	-0.033	0.021	4
25	83	-81.9	-40.5	-86.2	-44.6	-78.2	-37.0	-0.092	0.018	-0.072	0.017	21.3	-0.030	0.009	6
26		-74.3	-47.6	-78.2	-51.0	-71.0	-44.6	-0.082	0.017	-0.072	0.017	23.0	-0.010	0.007	6
27	99	-71.4	-28.7	-76.6	-32.6	-67.4	-25.0	-0.070	0.020	-0.059	0.020	11.1	0.038	0.013	5
28		-58.3	-70.0	-62.2	-74.2	-53.8	-65.8	-0.150	0.011	-0.081	0.009	39.0	0.019	0.006	6
29	41	-51.8	-82.6	-55.4	-86.6	-48.6	-78.6	-0.102	0.020	-0.133	0.020	11.7	-0.020	0.018	5
30	51	-48.9	-68.3	-55.0	-72.6	-44.2	-63.0	-0.057	0.011	-0.094	0.010	34.2	-0.012	0.004	6
31	72	-43.0	-50.2	-46.2	-52.6	-39.0	-46.2	-0.080	0.034	-0.032	0.035	1.4	-0.033	0.025	5
32	60	-36.6	-58.6	-40.2	-61.8	-32.6	-55.0	-0.071	0.019	-0.137	0.024	8.1	-0.011	0.012	6
33	34	-32.2	-88.2	-37.4	-91.8	-27.8	-83.0	-0.030	0.015	-0.104	0.016	11.5	-0.006	0.007	6
34	63	-29.8	-57.8	-33.4	-61.0	-25.4	-53.8	-0.038	0.025	-0.056	0.020	10.1	0.030	0.010	5
35		-15.9	-46.6	-20.2	-50.2	-12.2	-43.4	0.054	0.021	-0.012	0.015	14.7	0.056	0.009	5
36	53	-13.4	-68.6	-17.4	-75.4	-9.8	-64.2	0.049	0.024	-0.119	0.028	10.6	-0.032	0.011	5
37	57	-8.8	-65.1	-12.2	-69.0	-1.8	-60.6	-0.014	0.031	-0.049	0.023	16.3	0.010	0.013	5
38		-8.0	-51.6	-11.4	-55.0	-5.4	-48.2	-0.058	0.023	-0.023	0.030	11.2	0.030	0.016	5
39	32	-3.0	-97.4	-7.0	-101.8	1.0	-93.4	-0.019	0.019	-0.201	0.017	6.6	-0.034	0.010	6
40	39	-0.2	-82.6	-4.2	-87.4	4.2	-78.2	0.016	0.031	-0.111	0.018	4.7	-0.009	0.014	5
41	64	-0.2	-55.4	-3.4	-59.0	4.6	-51.8	0.075	0.030	-0.021	0.031	12.1	-0.051	0.016	5
42	27	4.5	-95.8	-0.2	-102.2	7.8	-93.8	0.021	0.014	-0.173	0.012	14.1	0.021	0.008	6
43	92	7.2	-31.5	5.0	-34.2	10.2	-28.2	-0.036	0.021	0.067	0.021	39.6	0.007	0.014	5
44	29	13.5	-94.3	8.2	-98.2	18.6	-90.2	-0.012	0.010	-0.148	0.006	55.6	0.025	0.003	6
45	87	15.8	-38.6	12.6	-42.2	19.4	-33.8	0.006	0.013	-0.127	0.013	52.2	0.009	0.007	6
46		17.2	-59.5	13.8	-62.6	20.2	-56.6	0.102	0.042	-0.015	0.046	18.7	0.128	0.051	2
47	30	18.6	-92.0	16.2	-93.4	23.0	-87.0	0.007	0.017	-0.090	0.014	16.5	0.041	0.008	6
48		21.2	-53.9	19.0	-56.6	23.4	-51.0	-0.063	0.028	-0.040	0.028	3.1	-0.002	0.025	5
49	48	27.9	-74.7	22.2	-80.2	33.0	-70.6	0.023	0.012	-0.148	0.009	31.2	0.034	0.006	6
50	40	28.6	-87.8	24.6	-89.8	33.8	-82.6	0.050	0.028	-0.153	0.019	3.3	0.006	0.020	5
51	28	32.7	-95.0	28.6	-100.6	36.6	-91.8	0.035	0.014	-0.110	0.011	16.6	-0.029	0.005	6
52		34.2	-53.6	30.6	-56.2	38.2	-50.6	0.137	0.064	-0.070	0.038	4.5	0.003	0.034	4
53	98	34.8	-28.3	32.2	-30.6	37.8	-25.8	0.109	0.027	0.026	0.029	12.1	0.077	0.018	5
54		35.6	-36.5	33.4	-39.8	37.8	-33.4	0.158	0.023	0.086	0.034	9.4	0.057	0.013	4
55	47	37.8	-75.4	33.8	-79.4	40.6	-73.0	0.029	0.022	-0.049	0.017	16.8	0.058	0.013	5
56	84	39.0	-41.6	36.6	-44.6	41.4	-39.0	0.093	0.014	-0.134	0.015	13.0	-0.026	0.013	6
57	25	39.1	-97.0	35.0	-104.6	44.2	-94.2	-0.028	0.015	-0.094	0.015	19.2	-0.049	0.010	6
58	95	40.2	-33.0	36.6	-36.2	43.4	-30.2	0.103	0.021	-0.053	0.022	12.5	0.016	0.018	5
59	52	46.9	-66.0	43.0	-70.2	51.0	-61.4	0.007	0.011	-0.031	0.014	32.9	0.012	0.007	6
60	33	47.6	-93.0	43.4	-99.4	53.4	-87.8	0.002	0.011	-0.114	0.015	19.2	0.008	0.005	6
61	42	47.8	-75.4	45.0	-78.2	52.6	-71.8	0.035	0.016	-0.025	0.017	13.0	-0.041	0.011	6
62	66	58.4	-52.5	54.6	-56.6	61.8	-49.4	0.020	0.036	0.091	0.028	8.9	-0.011	0.013	5

TABLE 3—*Continued*

Knot	$Knot_T$	x	y	Box_{x1}	Box_{y1}	Box_{x2}	Box_{y2}	V_x	δV_x	V_y	δV_y	B	$\frac{\Delta B}{B}$	$\delta\frac{\Delta B}{B}$	#
63	45	59.0	-78.2	54.6	-82.2	63.0	-73.0	0.072	0.019	-0.125	0.016	21.7	0.020	0.009	6
64	37	60.1	-85.5	56.6	-89.0	63.8	-83.0	0.046	0.027	-0.109	0.028	8.9	-0.088	0.020	6
65	89	63.0	-37.0	58.6	-41.4	67.4	-33.0	0.067	0.013	-0.027	0.019	6.8	-0.030	0.009	6
66	74	63.4	-47.8	59.0	-51.8	67.4	-43.8	0.005	0.029	-0.013	0.029	9.0	0.040	0.015	5
67		65.8	-75.4	62.2	-79.0	70.6	-71.0	0.100	0.029	-0.044	0.026	11.2	0.004	0.016	5
68		73.4	-37.4	70.2	-39.8	75.8	-34.2	0.017	0.029	-0.001	0.015	11.6	0.032	0.013	5
69		74.6	-71.0	71.8	-74.2	76.6	-68.2	0.110	0.016	-0.125	0.013	12.1	-0.008	0.010	6
70	86	77.8	-38.6	75.0	-43.4	81.0	-34.2	0.097	0.019	-0.016	0.012	14.8	0.041	0.005	6
71	43	82.6	-76.2	77.4	-83.0	89.0	-69.8	0.080	0.006	-0.030	0.008	45.9	0.012	0.003	6
72	55	84.2	-66.6	79.4	-70.6	88.2	-62.6	0.173	0.018	-0.104	0.013	13.9	0.018	0.008	6
73	26	90.8	-100.2	87.0	-104.2	96.2	-91.8	0.182	0.022	-0.123	0.027	10.0	0.061	0.013	5
74	62	91.8	-56.6	88.6	-61.4	95.4	-52.2	0.039	0.018	-0.037	0.034	7.5	-0.007	0.010	5
75	81	92.2	-43.0	87.0	-45.4	95.8	-37.4	-0.019	0.019	-0.070	0.018	22.9	0.016	0.007	6
76	36	95.5	-85.5	88.6	-92.6	101.4	-81.0	0.217	0.025	-0.191	0.021	6.6	-0.005	0.010	6
77	80	97.5	-44.4	95.0	-47.4	101.0	-41.4	0.104	0.021	-0.131	0.016	16.5	0.070	0.011	5
78	54	104.1	-66.7	100.2	-74.2	108.6	-62.6	0.066	0.009	-0.058	0.014	24.3	0.030	0.005	6
79	23	106.6	-101.4	100.2	-108.6	113.8	-93.0	0.158	0.016	-0.227	0.018	7.5	0.018	0.006	6
80	96	110.2	-34.2	106.6	-39.8	113.8	-29.4	0.039	0.009	-0.085	0.016	42.0	0.045	0.004	6
81		121.2	-31.9	117.8	-36.2	125.4	-29.0	0.133	0.022	0.000	0.021	20.4	0.017	0.012	5
82	209	-165.0	35.0	-167.8	29.4	-161.8	40.6	-0.278	0.014	0.080	0.022	5.8	0.041	0.008	6
83	194	-162.6	24.2	-166.2	18.2	-159.0	27.8	-0.216	0.013	0.008	0.029	6.8	0.066	0.009	5
84	200	-150.6	29.8	-155.8	25.0	-147.0	34.2	-0.146	0.043	0.063	0.033	6.5	0.058	0.014	3
85		-148.1	52.2	-150.6	49.8	-145.4	55.8	-0.247	0.024	0.177	0.026	12.0	0.110	0.019	5
86	230	-147.1	47.5	-150.6	43.8	-143.8	50.6	-0.215	0.009	0.090	0.011	41.0	0.032	0.006	6
87	220	-142.2	40.7	-145.8	37.4	-138.6	44.2	-0.150	0.014	0.058	0.017	9.7	0.005	0.009	6
88		-141.4	46.2	-144.2	43.4	-138.6	49.4	-0.174	0.014	0.141	0.018	16.7	0.045	0.008	6
89	118	-140.2	-16.3	-143.4	-19.4	-138.2	-12.6	-0.292	0.016	-0.081	0.018	17.9	-0.013	0.012	5
90	120	-136.2	-16.6	-138.2	-24.6	-132.2	-11.0	-0.232	0.011	-0.002	0.016	12.9	0.058	0.006	6
91	206	-136.2	30.2	-139.4	26.6	-132.6	33.8	-0.089	0.042	0.102	0.049	2.9	-0.031	0.037	4
92	104	-132.5	-27.3	-135.8	-31.0	-129.0	-24.2	-0.201	0.018	-0.129	0.018	8.0	0.002	0.011	6
93	123	-127.8	-16.6	-131.0	-19.8	-124.6	-12.6	-0.271	0.018	-0.021	0.017	31.9	-0.028	0.012	6
94	186	-121.4	19.2	-128.6	11.8	-117.4	25.8	-0.152	0.005	-0.004	0.007	21.1	0.041	0.002	6
95	201	-113.4	29.4	-116.6	25.8	-111.4	33.4	-0.138	0.033	-0.089	0.027	2.1	0.035	0.020	5
96		-110.2	-27.8	-113.8	-31.4	-107.8	-23.4	-0.147	0.017	-0.082	0.027	3.3	0.065	0.017	5
97		-109.0	26.6	-111.8	23.4	-106.6	29.0	-0.145	0.140	0.053	0.160	1.1	0.236	0.153	2
98	157	-108.2	3.4	-112.2	1.0	-104.6	6.6	-0.079	0.015	0.015	0.009	13.1	0.016	0.008	6
99	126	-107.4	-12.6	-112.6	-17.8	-105.0	-10.2	-0.082	0.019	-0.017	0.026	5.3	0.030	0.012	5
100	150	-103.4	-2.0	-107.0	-6.2	-99.0	2.2	-0.129	0.009	0.024	0.009	53.6	0.020	0.005	6
101		-100.2	28.6	-105.4	24.6	-96.2	32.6	-0.125	0.023	0.057	0.023	3.8	0.027	0.017	5
102	130	-96.2	-10.2	-101.8	-17.0	-92.6	-7.4	-0.116	0.022	-0.037	0.016	13.9	0.011	0.010	5
103	152	-94.9	-1.7	-97.4	-3.8	-91.8	1.8	-0.157	0.013	0.001	0.011	18.5	0.036	0.008	6
104	181	-90.7	17.4	-93.8	13.4	-87.4	21.0	-0.120	0.016	0.028	0.018	13.6	0.001	0.009	6
105	217	-88.6	38.2	-92.2	34.2	-85.0	42.2	-0.134	0.020	-0.011	0.031	8.4	0.009	0.011	6
106	136	-86.9	-7.3	-92.6	-12.2	-82.6	-3.4	-0.126	0.016	-0.013	0.011	26.7	0.029	0.005	6
107	198	-86.2	25.4	-90.2	21.0	-82.6	31.0	-0.077	0.008	-0.036	0.012	18.6	0.029	0.004	6
108	211	-76.6	35.8	-81.0	27.8	-72.6	39.8	-0.102	0.013	0.038	0.020	3.4	0.017	0.012	6
109	124	-75.4	-13.4	-79.4	-18.2	-73.0	-9.0	-0.085	0.009	-0.077	0.011	17.8	0.023	0.005	6
110	179	-72.2	13.8	-78.2	9.8	-68.6	18.2	-0.115	0.032	-0.015	0.027	6.8	-0.014	0.013	5
111	121	-67.0	-15.4	-70.6	-19.0	-62.2	-10.2	0.001	0.019	-0.021	0.020	8.6	0.012	0.010	4
112	228	-66.6	44.6	-69.4	41.0	-61.0	49.0	-0.082	0.014	0.063	0.016	7.2	0.022	0.010	6
113	141	-64.5	-6.4	-67.0	-9.4	-61.0	-3.0	0.078	0.046	-0.064	0.048	7.2	0.004	0.030	4
114		-61.8	50.6	-65.0	47.0	-58.6	53.8	-0.063	0.019	0.138	0.026	9.8	0.049	0.013	5
115	214	-59.8	36.2	-65.0	30.2	-56.2	39.4	0.036	0.016	0.035	0.018	8.3	0.009	0.008	6
116	156	-56.6	3.4	-59.4	0.2	-51.8	7.4	-0.076	0.021	0.033	0.013	8.6	-0.019	0.011	6
117	170	-42.6	9.8	-49.0	5.0	-40.2	13.8	-0.040	0.021	-0.037	0.022	3.9	-0.021	0.013	6
118	148	-33.8	-3.2	-37.8	-7.4	-30.6	0.2	-0.017	0.047	0.014	0.036	4.1	0.034	0.039	4
119		-33.4	17.8	-37.4	14.6	-31.0	21.0	-0.055	0.023	-0.179	0.025	7.3	-0.018	0.015	6
120	192	-30.2	22.2	-33.0	18.6	-26.2	26.6	-0.009	0.015	-0.022	0.017	8.2	-0.033	0.012	6
121	234	-22.2	49.8	-27.0	45.0	-17.0	53.8	0.100	0.025	-0.020	0.026	10.1	0.009	0.011	5
122	138	-17.8	-9.5	-22.2	-13.4	-14.2	-6.2	0.011	0.036	0.008	0.029	5.9	0.010	0.013	4
123	191	-15.8	22.2	-19.0	15.8	-9.8	25.4	-0.010	0.019	0.065	0.018	8.0	0.013	0.010	6
124	105	-12.7	-26.2	-17.0	-31.4	-9.8	-23.4	-0.101	0.071	-0.049	0.057	4.5	-0.072	0.036	4

TABLE 3—*Continued*

Knot	$Knot_T$	x	y	Box_{x1}	Box_{y1}	Box_{x2}	Box_{y2}	V_x	δV_x	V_y	δV_y	B	$\frac{\Delta B}{B}$	$\delta\frac{\Delta B}{B}$	#
125	162	-1.0	5.0	-4.2	1.4	2.2	7.8	0.051	0.024	-0.013	0.019	5.5	0.001	0.016	6
126	112	1.3	-22.7	-2.2	-27.0	5.8	-17.8	0.109	0.019	-0.002	0.022	16.6	-0.027	0.009	6
127		2.6	28.6	-0.6	25.4	6.2	32.6	0.004	0.013	0.006	0.013	15.1	0.025	0.010	6
128	210	4.6	35.8	0.6	33.8	9.0	41.8	0.058	0.013	0.048	0.011	13.7	-0.011	0.007	6
129	173	5.0	13.0	1.0	9.4	9.0	17.0	0.014	0.010	-0.016	0.013	16.2	-0.022	0.006	6
130		7.0	31.8	4.6	28.6	11.0	35.4	0.035	0.012	0.054	0.016	13.9	0.025	0.008	6
131	119	7.7	-18.5	4.6	-21.4	11.4	-15.4	0.017	0.026	-0.015	0.023	3.6	-0.033	0.017	6
132	145	9.0	-2.2	5.0	-4.2	11.4	-0.2	0.075	0.028	0.059	0.031	47.4	0.061	0.029	4
133	164	9.4	6.6	5.8	3.8	11.4	10.2	0.041	0.016	-0.032	0.020	18.6	-0.021	0.009	6
134	188	11.0	21.0	6.6	17.0	14.6	24.6	0.052	0.021	-0.050	0.019	11.2	-0.028	0.011	5
135		11.0	-7.0	8.6	-11.0	13.0	-5.0	0.054	0.019	-0.089	0.024	38.2	0.035	0.020	4
136		13.3	7.1	10.6	3.8	17.0	10.6	0.049	0.011	-0.026	0.012	39.6	0.021	0.007	6
137	232	20.6	45.0	17.0	41.8	24.2	49.4	0.101	0.020	-0.062	0.015	13.1	0.004	0.008	6
138	223	21.4	40.6	17.8	37.4	24.6	43.8	0.035	0.021	-0.065	0.016	5.9	0.019	0.012	6
139	132	22.9	-13.2	19.4	-16.2	26.2	-9.0	0.171	0.056	-0.105	0.032	5.1	0.122	0.036	3
140	169	28.9	9.1	26.2	6.6	32.2	12.6	0.101	0.036	-0.061	0.040	5.1	0.034	0.042	4
141		33.3	-18.6	30.2	-21.4	36.2	-14.2	0.026	0.019	-0.028	0.021	19.2	0.111	0.015	5
142		35.1	-4.4	31.8	-7.8	38.2	-1.4	0.030	0.046	-0.258	0.026	16.3	0.121	0.016	4
143		35.4	-11.0	31.4	-14.6	41.4	-7.4	0.023	0.052	-0.059	0.036	9.7	0.055	0.026	3
144	193	36.6	25.0	34.2	22.2	40.6	29.0	0.049	0.015	0.031	0.016	8.7	0.010	0.010	6
145	224	36.6	41.4	32.2	37.0	39.8	44.6	0.001	0.012	-0.054	0.015	12.2	-0.027	0.007	6
146	111	38.6	-23.8	35.8	-26.2	40.6	-20.6	0.084	0.020	-0.059	0.019	21.5	-0.095	0.016	5
147		39.0	47.4	35.4	44.6	42.2	50.6	0.092	0.021	0.054	0.020	8.8	0.012	0.012	6
148		39.8	-16.2	37.0	-19.8	43.4	-12.6	0.057	0.021	-0.008	0.028	5.6	-0.003	0.016	5
149		41.0	20.6	39.0	17.8	45.4	25.8	0.068	0.018	-0.092	0.024	6.7	0.026	0.011	6
150	109	43.0	-23.8	40.6	-26.6	46.2	-21.0	0.122	0.026	-0.037	0.025	41.7	-0.029	0.017	5
151	212	48.2	35.9	45.0	32.6	50.6	39.0	0.047	0.021	0.001	0.021	4.3	-0.041	0.019	5
152	235	50.2	50.6	45.4	46.2	53.4	54.6	0.023	0.018	-0.040	0.019	23.8	0.033	0.006	6
153		53.4	-2.2	49.8	-5.4	57.4	1.8	0.058	0.018	0.008	0.019	13.2	0.069	0.014	5
154	102	55.8	-25.8	53.4	-33.0	60.2	-19.8	0.086	0.012	0.051	0.017	10.9	0.054	0.006	6
155	204	56.2	33.8	51.0	31.0	60.2	37.0	0.104	0.025	0.058	0.020	17.7	-0.099	0.017	5
156	215	62.2	38.6	59.4	35.4	65.8	41.8	0.034	0.022	0.031	0.020	17.3	0.029	0.010	6
157		62.9	-2.6	60.2	-5.4	65.0	-0.6	0.078	0.020	-0.014	0.021	20.0	0.062	0.016	5
158	154	65.4	0.4	63.0	-2.2	68.6	3.4	0.057	0.019	-0.073	0.023	19.3	-0.003	0.013	6
159		66.1	-9.1	63.0	-13.8	69.8	-5.8	0.025	0.014	0.003	0.025	13.2	0.009	0.012	5
160	110	69.7	-23.8	65.0	-29.8	73.8	-18.6	-0.007	0.011	-0.010	0.015	31.7	-0.032	0.007	6
161		71.1	15.2	69.8	13.8	74.2	17.8	0.212	0.127	0.087	0.138	2.9	0.181	0.211	2
162	203	75.1	31.1	70.6	27.0	78.6	34.2	0.073	0.016	-0.005	0.014	23.7	-0.023	0.011	6
163	117	76.0	-18.8	72.6	-21.8	79.8	-15.4	-0.019	0.010	-0.056	0.012	32.5	0.026	0.006	6
164	163	76.6	4.6	73.0	1.8	81.8	9.4	-0.089	0.025	0.010	0.020	45.3	0.086	0.010	5
165	207	80.9	32.8	77.8	29.4	84.2	35.8	0.085	0.016	-0.044	0.017	8.1	-0.001	0.015	6
166	147	81.4	3.0	79.4	-2.2	85.0	5.4	-0.003	0.057	0.122	0.059	24.1	0.080	0.029	3
167	172	83.0	12.6	77.8	8.2	89.0	15.4	0.126	0.031	-0.019	0.014	18.9	0.007	0.011	5
168	144	87.0	-2.2	84.6	-7.0	91.4	0.2	0.054	0.023	-0.005	0.021	13.2	-0.005	0.013	5
169	216	87.9	37.2	84.2	33.8	91.4	40.6	-0.012	0.015	-0.091	0.012	19.3	0.006	0.008	6
170	122	91.4	-17.4	86.2	-22.6	97.4	-12.2	0.070	0.016	0.014	0.023	13.9	0.004	0.005	6
171	227	91.4	43.8	88.2	40.2	93.8	46.2	0.142	0.023	-0.038	0.017	10.7	0.010	0.010	6
172	160	93.8	5.0	89.0	0.2	96.6	6.6	-0.006	0.037	-0.069	0.024	14.5	0.024	0.016	5
173	180	97.2	17.4	94.2	14.6	99.8	21.0	0.063	0.026	0.004	0.029	4.2	0.004	0.019	5
174		98.9	8.6	96.2	5.8	101.0	11.4	0.110	0.050	-0.043	0.046	17.0	0.089	0.032	4
175	171	99.8	12.6	97.0	10.6	103.4	16.2	0.102	0.020	-0.043	0.025	4.7	-0.062	0.021	6
176	131	100.0	-8.5	96.6	-10.2	101.8	-5.4	-0.014	0.035	0.100	0.035	10.0	0.065	0.038	4
177	233	103.4	49.4	99.0	45.4	107.0	52.6	0.138	0.028	-0.033	0.018	6.5	-0.019	0.011	6
178	187	107.0	20.2	103.8	17.4	109.8	23.0	-0.076	0.060	0.127	0.140	8.0	0.104	0.050	2
179		107.8	41.8	105.0	38.6	111.4	45.4	0.089	0.017	0.013	0.017	5.6	-0.013	0.011	6
180		109.5	25.8	106.6	22.2	113.8	29.0	-0.003	0.020	-0.017	0.021	17.0	0.068	0.014	5
181		110.2	-25.8	107.4	-29.0	113.8	-23.4	0.129	0.029	0.011	0.030	21.0	0.050	0.025	4
182		111.0	-14.6	107.4	-17.4	113.8	-11.0	0.046	0.022	-0.028	0.019	8.9	0.021	0.014	5
183		111.4	17.6	108.2	13.8	115.0	21.0	0.070	0.028	-0.063	0.035	14.6	0.116	0.018	4
184		113.0	46.6	109.4	43.4	115.4	50.2	0.152	0.020	-0.037	0.022	9.3	-0.018	0.017	6
185		114.4	37.1	111.0	34.2	118.2	40.2	-0.023	0.022	-0.012	0.019	21.9	0.023	0.013	5
186	161	116.2	7.1	112.2	2.2	121.4	11.0	-0.052	0.023	0.001	0.019	41.2	0.016	0.008	5

TABLE 3—*Continued*

Knot	$Knot_T$	x	y	Box_{x1}	Box_{y1}	Box_{x2}	Box_{y2}	V_x	δV_x	V_y	δV_y	B	$\frac{\Delta B}{B}$	$\delta\frac{\Delta B}{B}$	#
187	127	117.2	-13.2	111.8	-19.4	119.8	-10.6	0.070	0.013	-0.020	0.013	12.9	-0.003	0.007	6
188	199	117.8	27.0	115.0	24.2	121.4	30.6	0.044	0.028	-0.067	0.029	11.2	0.035	0.024	5
189	177	119.4	14.9	115.8	11.8	122.2	18.2	0.097	0.013	-0.019	0.014	25.1	0.047	0.008	6
190	231	120.6	44.2	117.0	41.8	123.4	47.0	0.122	0.027	0.014	0.034	19.9	0.009	0.018	4
191	218	121.4	40.2	118.2	37.4	124.2	43.4	0.012	0.029	0.130	0.040	18.4	-0.034	0.024	5
192		121.4	19.6	117.8	17.4	125.0	23.0	0.007	0.060	-0.017	0.044	23.9	-0.009	0.040	3
193		123.9	-21.5	121.0	-23.8	126.6	-18.6	0.075	0.024	0.015	0.017	22.2	0.011	0.013	4
194		124.2	36.2	120.2	32.2	127.4	39.8	0.022	0.017	0.134	0.016	25.2	0.043	0.008	6
195	135	125.0	-9.0	121.0	-12.2	128.2	-5.4	0.045	0.017	-0.045	0.018	15.2	-0.039	0.015	6
196		127.9	-25.5	124.6	-29.0	131.0	-22.2	0.130	0.013	-0.001	0.014	27.9	0.012	0.009	5
197	129	128.2	-13.4	124.6	-15.8	130.2	-11.0	0.060	0.019	-0.133	0.018	19.7	0.018	0.013	6
198	142	129.7	-4.5	126.6	-7.8	132.2	-2.2	0.051	0.020	-0.019	0.021	17.8	-0.043	0.026	6
199		130.6	-9.8	127.8	-13.0	134.2	-7.0	0.111	0.012	-0.139	0.019	19.2	-0.007	0.012	6
200	226	131.8	43.4	128.6	40.6	135.0	46.6	0.101	0.027	0.025	0.036	7.8	-0.044	0.032	4
201		134.0	30.8	130.2	26.6	136.6	33.0	0.152	0.025	0.046	0.021	10.7	0.048	0.016	5
202	168	134.6	6.9	131.0	2.6	138.6	11.4	-0.200	0.019	-0.130	0.018	93.8	0.026	0.007	6
203		135.0	47.4	132.2	45.0	137.8	50.2	0.186	0.021	0.121	0.037	6.6	0.018	0.027	4
204		136.6	34.2	134.6	31.8	140.2	37.8	0.187	0.042	0.014	0.045	1.9	-0.088	0.057	5
205	151	137.4	1.0	134.2	-2.2	139.8	3.4	0.188	0.052	0.000	0.052	5.0	-0.044	0.055	3
206		137.4	12.2	134.6	9.8	141.0	16.2	0.192	0.029	-0.018	0.042	14.1	-0.027	0.028	3
207	202	144.6	30.6	139.0	24.6	147.8	35.8	0.181	0.013	0.014	0.017	9.5	-0.013	0.007	6
208		147.0	37.8	143.4	34.2	150.6	41.4	0.230	0.026	0.017	0.038	4.4	0.030	0.021	4
209	146	147.3	-1.6	143.4	-6.2	151.4	2.2	0.228	0.013	0.147	0.012	58.5	0.006	0.006	6
210	139	149.8	-7.1	147.4	-11.0	152.2	-5.0	0.102	0.012	0.036	0.014	19.0	-0.001	0.013	6
211	159	151.4	2.2	148.6	1.0	154.6	7.4	0.176	0.029	0.032	0.029	26.4	0.003	0.015	4
212	225	153.4	43.0	150.6	39.8	157.8	47.0	0.183	0.027	0.133	0.027	4.0	0.047	0.024	5
213	149	154.1	-1.8	150.2	-6.6	157.8	1.4	0.214	0.016	0.052	0.020	13.9	-0.034	0.015	6
214		155.6	14.3	151.8	10.6	159.0	18.2	0.231	0.013	0.017	0.017	13.7	0.030	0.006	6
215		186.2	8.6	181.8	4.6	190.6	12.2	0.376	0.048	-0.106	0.049	2.7	0.043	0.039	4
216		-181.4	109.8	-184.2	107.0	-177.4	113.0	-0.345	0.016	0.269	0.024	6.9	0.137	0.011	5
217		-180.2	97.0	-183.8	93.4	-177.0	100.6	-0.247	0.042	0.087	0.040	2.1	0.078	0.033	4
218		-179.8	64.6	-183.0	61.8	-176.2	67.4	-0.368	0.021	0.141	0.025	9.0	0.115	0.008	5
219		-178.3	70.8	-181.4	67.8	-174.6	74.2	-0.217	0.043	0.024	0.024	4.1	0.132	0.018	4
220	242	-157.4	56.6	-163.0	52.2	-155.4	59.4	-0.260	0.011	0.157	0.019	29.7	0.046	0.006	6
221		-151.8	104.2	-154.2	101.8	-149.8	108.2	-0.297	0.053	0.274	0.047	3.1	0.062	0.030	4
222	264	-148.2	70.6	-151.0	66.2	-143.4	74.6	-0.240	0.010	0.054	0.018	8.4	-0.003	0.007	6
223		-146.6	107.8	-150.6	103.4	-142.2	112.2	-0.190	0.033	0.133	0.032	5.3	0.103	0.021	4
224	318	-138.6	127.8	-143.0	122.2	-135.0	131.0	-0.112	0.013	0.140	0.020	6.4	0.048	0.010	6
225	253	-137.0	62.2	-141.0	58.6	-133.4	65.8	-0.292	0.042	-0.015	0.042	2.6	-0.042	0.029	3
226	297	-125.0	97.8	-130.2	94.2	-121.0	104.2	-0.253	0.044	0.162	0.036	3.5	0.023	0.014	4
227		-123.4	121.8	-127.0	119.0	-119.0	125.4	-0.118	0.032	0.173	0.027	4.3	0.047	0.023	5
228	315	-119.4	117.0	-125.4	111.8	-115.0	122.2	-0.180	0.019	0.184	0.015	8.5	0.019	0.008	6
229	273	-89.0	75.8	-94.6	72.2	-84.2	80.2	-0.096	0.014	0.121	0.012	17.4	-0.015	0.005	6
230	257	-88.6	64.6	-91.8	60.6	-84.6	68.6	-0.164	0.038	0.053	0.016	13.5	0.013	0.009	4
231	244	-80.6	56.6	-83.8	53.4	-77.8	60.2	-0.067	0.017	0.110	0.016	7.3	-0.047	0.010	6
232	289	-77.8	93.0	-82.6	89.8	-74.2	98.6	-0.063	0.029	0.099	0.029	7.0	0.039	0.012	5
233	267	-74.2	69.0	-77.8	65.8	-68.2	72.6	-0.053	0.015	0.107	0.012	16.8	-0.042	0.008	6
234	275	-69.4	76.2	-77.4	72.6	-65.4	80.6	-0.094	0.019	0.124	0.010	19.3	-0.001	0.004	6
235	278	-61.4	78.2	-66.6	72.6	-52.6	81.0	-0.072	0.012	0.154	0.008	45.3	0.045	0.003	6
236	263	-57.4	68.2	-61.4	64.2	-55.0	71.0	-0.062	0.016	0.078	0.017	10.7	0.039	0.012	6
237	300	-50.2	103.4	-54.6	99.0	-46.6	107.8	-0.085	0.027	0.097	0.020	5.1	0.011	0.010	6
238	279	-48.2	77.4	-51.4	73.8	-43.8	80.2	-0.104	0.017	0.147	0.015	20.2	0.035	0.009	6
239	317	-42.2	123.0	-46.6	118.6	-38.6	126.6	-0.078	0.014	0.077	0.023	7.7	0.021	0.010	6
240		-38.6	90.6	-42.6	86.6	-35.8	95.4	-0.021	0.013	0.076	0.017	16.5	0.035	0.006	6
241		-33.4	75.0	-37.0	71.0	-30.6	77.8	-0.053	0.034	0.080	0.036	11.6	0.085	0.018	4
242	283	-31.0	84.6	-35.4	81.4	-27.4	88.6	-0.070	0.015	0.101	0.011	16.6	0.002	0.007	6
243		-30.6	94.2	-35.8	91.0	-25.4	98.2	-0.039	0.027	0.125	0.016	14.8	0.089	0.010	5
244	316	-29.0	120.6	-33.0	117.8	-24.6	125.8	0.068	0.030	0.159	0.030	6.0	0.038	0.021	4
245	252	-16.6	62.2	-21.0	57.8	-12.2	66.2	-0.058	0.021	0.121	0.017	9.7	0.034	0.008	5
246	272	-16.6	75.4	-19.8	72.6	-13.4	79.8	-0.029	0.018	0.123	0.019	12.3	0.037	0.011	6
247	310	-14.6	110.2	-19.8	108.2	-11.0	114.6	-0.034	0.031	0.105	0.020	9.1	-0.003	0.014	5
248		-13.8	97.8	-17.4	94.2	-10.2	101.0	0.048	0.017	0.155	0.012	24.4	0.037	0.008	5

TABLE 3—*Continued*

Knot	Knot$_T$	x	y	Box$_{x1}$	Box$_{y1}$	Box$_{x2}$	Box$_{y2}$	V_x	δV_x	V_y	δV_y	B	$\frac{\Delta B}{B}$	$\delta\frac{\Delta B}{B}$	#
249	294	-7.4	100.2	-11.4	97.0	-3.4	103.8	-0.002	0.029	0.245	0.026	11.7	-0.031	0.020	5
250	314	-7.4	115.0	-10.6	113.0	-4.6	119.0	-0.055	0.107	0.134	0.100	2.1	0.037	0.076	2
251		-2.2	59.4	-5.8	57.4	-0.6	62.6	-0.015	0.022	0.056	0.019	2.8	-0.078	0.028	6
252	276	-0.2	75.8	-3.8	71.8	3.4	79.8	-0.006	0.018	0.111	0.017	11.6	-0.022	0.010	6
253	292	0.2	99.8	-3.8	94.6	3.0	102.6	-0.127	0.065	0.088	0.066	5.0	-0.175	0.053	3
254	254	0.6	63.4	-2.6	61.0	3.4	66.6	0.023	0.024	0.015	0.019	2.6	-0.035	0.022	6
255		3.8	106.2	0.6	103.0	5.4	110.2	0.026	0.024	0.110	0.025	10.2	0.024	0.014	5
256	290	7.0	92.2	1.0	87.0	11.8	99.0	-0.039	0.013	0.019	0.015	20.1	0.018	0.005	6
257	309	7.4	108.2	5.0	104.2	9.8	111.8	0.083	0.019	0.085	0.016	11.1	-0.014	0.009	6
258	308	11.4	108.6	9.0	105.4	13.8	111.8	0.009	0.038	0.181	0.044	4.9	-0.001	0.025	4
259	343	13.4	76.6	9.0	73.0	17.4	80.6	0.102	0.007	0.076	0.007	70.4	0.084	0.003	6
260		17.0	101.4	13.0	97.8	21.4	105.4	-0.058	0.039	0.191	0.026	9.3	-0.003	0.018	4
261	277	21.0	72.6	16.6	69.8	24.6	75.8	0.066	0.015	0.068	0.009	40.0	0.049	0.006	6
262	237	25.4	53.4	22.2	50.6	28.6	57.4	0.048	0.021	0.052	0.041	14.2	0.003	0.012	4
263	302	27.8	104.2	24.2	101.0	31.4	108.2	0.067	0.017	0.083	0.020	11.6	-0.009	0.012	6
264	271	31.0	70.2	27.0	67.4	33.8	73.4	0.110	0.015	-0.118	0.017	29.4	0.004	0.009	6
265		31.0	96.6	26.6	93.0	33.4	100.2	0.029	0.021	0.176	0.016	36.0	0.052	0.012	5
266	293	32.6	100.2	31.0	98.6	35.8	103.8	0.056	0.065	0.111	0.076	3.6	-0.100	0.142	3
267	313	32.6	110.6	30.2	108.2	37.4	119.4	0.079	0.021	0.044	0.029	15.2	-0.023	0.008	5
268	281	34.6	79.0	31.8	77.0	37.4	83.0	0.064	0.020	0.175	0.019	6.2	-0.061	0.015	6
269		39.4	81.0	36.6	77.8	42.6	84.2	0.109	0.024	0.141	0.032	7.3	-0.029	0.023	6
270		41.0	110.6	37.0	106.6	44.2	113.0	0.208	0.042	0.149	0.023	9.8	-0.074	0.029	5
271	298	42.2	97.4	38.2	93.0	47.0	101.8	0.026	0.021	0.052	0.028	27.3	0.012	0.010	5
272	265	43.0	72.6	39.0	69.0	47.4	75.0	0.048	0.022	0.132	0.021	5.7	0.001	0.020	6
273	256	57.0	66.2	53.0	62.6	60.2	69.8	0.054	0.012	0.065	0.019	13.5	-0.042	0.008	6
274	311	57.8	111.8	54.2	109.4	60.6	115.4	0.109	0.054	0.191	0.065	2.7	0.024	0.043	3
275	305	67.4	104.2	63.4	100.6	71.8	107.8	0.076	0.027	0.053	0.024	43.5	0.024	0.009	5
276	243	71.8	53.8	67.8	50.2	75.4	56.6	0.081	0.015	0.041	0.013	49.1	0.028	0.006	6
277	280	79.0	78.2	75.8	74.2	81.8	80.6	0.117	0.018	0.057	0.012	12.3	0.045	0.009	5
278	247	79.4	57.0	75.4	53.0	83.4	61.4	0.066	0.012	0.041	0.008	46.9	-0.016	0.004	6
279		85.0	85.0	80.2	81.8	87.8	89.4	0.137	0.023	0.027	0.016	17.9	0.010	0.009	6
280	251	97.4	59.8	93.4	56.6	101.0	63.0	0.089	0.017	0.050	0.016	39.9	0.018	0.009	6
281		98.2	66.6	94.6	64.2	99.4	69.4	0.118	0.026	0.118	0.025	17.2	-0.002	0.018	4
282		101.0	65.8	99.0	64.2	102.6	69.0	0.096	0.022	0.076	0.016	23.6	0.052	0.011	6
283	259	104.6	65.4	102.2	62.2	105.8	68.6	0.021	0.035	-0.007	0.019	14.7	0.013	0.016	5
284	282	107.4	81.4	104.6	79.4	111.0	85.4	0.120	0.019	0.060	0.022	13.5	0.034	0.015	5
285		107.8	66.2	106.2	63.4	110.6	69.0	0.128	0.030	-0.069	0.026	19.2	0.017	0.018	4
286	250	114.6	58.2	111.0	54.6	118.6	62.6	0.091	0.016	-0.045	0.015	18.2	-0.004	0.007	6
287		130.4	53.3	127.8	49.8	133.0	56.6	0.184	0.026	0.064	0.026	28.3	0.049	0.015	4
288	335	-5.4	149.8	-10.6	145.8	-1.8	155.0	-0.025	0.014	0.114	0.013	51.6	0.024	0.005	6
289	329	2.6	145.4	-2.2	143.4	6.6	149.4	-0.029	0.018	0.114	0.010	22.8	0.044	0.008	6
290		3.4	153.4	1.0	150.6	5.8	156.6	-0.010	0.013	0.140	0.023	1.0	-0.006	0.014	6
291	342	4.6	184.2	0.6	180.2	9.4	186.6	-0.018	0.014	0.315	0.007	27.1	0.054	0.005	6
292	323	7.8	140.2	5.8	129.4	19.4	142.2	0.009	0.012	0.208	0.012	7.9	-0.015	0.008	6
293		8.6	167.8	4.2	163.8	11.8	171.0	-0.094	0.043	0.280	0.033	2.4	-0.011	0.030	4
294	332	11.4	146.6	7.8	142.6	16.2	150.6	0.075	0.015	0.063	0.009	55.6	0.009	0.005	6
295	339	29.8	161.4	26.6	158.2	33.4	164.6	0.039	0.017	0.174	0.010	28.9	0.018	0.009	6
296	322	33.8	135.8	30.2	131.4	36.2	138.2	0.006	0.019	0.111	0.010	19.5	0.071	0.007	6
297	334	35.8	149.4	32.2	146.2	40.6	153.8	0.046	0.022	0.126	0.015	8.6	0.001	0.010	6
298	321	38.6	135.0	35.4	131.4	41.8	138.2	0.020	0.028	0.089	0.013	27.1	0.060	0.010	5
299	330	58.2	147.0	56.2	145.0	61.4	150.2	0.096	0.016	0.130	0.019	3.9	-0.044	0.015	6
300	324	59.8	140.6	55.8	137.4	63.8	144.6	0.128	0.011	0.217	0.011	39.0	0.065	0.004	6
301		65.0	146.2	63.0	143.8	67.8	149.4	0.100	0.021	0.069	0.020	7.3	-0.007	0.014	6
302	337	67.0	159.4	63.8	155.4	70.6	163.4	0.107	0.025	0.280	0.034	7.0	0.021	0.015	5
303	327	76.6	145.8	73.4	141.8	80.6	148.6	0.126	0.039	0.259	0.031	4.9	0.037	0.021	4
304	328	83.4	146.6	79.8	143.4	86.2	150.6	0.040	0.085	0.275	0.039	4.2	0.022	0.018	3

NOTES.—Col. 1.—Knot designation number. Col. (2).—Designation number of Tuffs 1986, for knots which are clearly in both samples. Col. (3).—Epoch 1987 knot position, measured in seconds of arc with respect to the optical expansion center at $\alpha(1950) = 23^h21^m11^s.90$, $\delta(1950) = +58°32'17''.6$ (van den Bergh & Kamper 1983). Col. (4).—Box defining the regression region used for each knot (arcseconds, with respect to the optical expansion center). Col. (5).—Proper motion in right ascension (arcseconds yr^{-1}). Col. (6).—Uncertainty in right ascension proper motion—68% confidence (arcseconds yr^{-1}). Col. (7).—Proper motion in declination (arcseconds yr^{-1}). Col. (8).—Uncertainty in declination motion—68% confidence (arcseconds yr^{-1}). Col. (9).—Estimate of knot brightness at $\lambda = 6$ cm (mJy beam^{-1}, epoch 1987). Col. (10).—Annual fractional brightness change relative to the large-scale ring (yr^{-1}). Col. (11).—Uncertainty in fractional brightness change—68% confidence (yr^{-1}). Col. (12).—Number of epochs of data used in multi-epoch determinations.

ture coverage (in practice, primarily the size of the unsampled hole in the inner u-v plane) introduces different sizes and depths of "negative bowls" into the reconstructed images. To first order, this may mimic a constant offset between two images. To second order, a radial increase in residuals, as measured from the center of the brightness distribution, can result from differencing two unequally sized Gaussian bowls.

To minimize variations between epochs that may arise from a variety of instrumental factors, the maps have been normalized with respect to the epoch 1987 image—the C-band image of highest quality in the archive. This normalization will remove the overall decrease in integrated flux density, expected to be $\sim 12\%$ over 13 yr (Baars et al. 1977), but will still allow us to see differential flux changes among the various emission components. A straightforward pixel-by-pixel linear regression to obtain a best-fit multiplicative gain and offset will be corrupted by real small-scale changes in the images, particularly over long time baselines. A better estimate is given by fitting brightnesses averaged in annuli about the center of the bright radio ring [at $\alpha(1950) = 23^{h}21^{m}9^{s}.4$, $\delta(1950) = +58°32'19''.8$], providing the annulus width is large in comparison with typical proper motions. Radial and constant terms were included in the fit to eliminate variations due to non-uniform aperture coverage.

The fits thus took the form $C_{\rm epoch} = S_{\rm epoch} * C_{87} + A_{\rm epoch} * R + {\rm constant}_{\rm epoch}$, where $C_{\rm epoch}$ represents the average brightness in an annulus of midradius R, and $S_{\rm epoch}$ is the gain scaling factor. The results of these fits are tabulated by Anderson (1993). The errors in normalized gain are $\approx 1\%$, typically much smaller than the random noise errors associated with these features.

Again, this normalization procedure effectively removes from our image archive any real secular brightness change the large-scale diffuse ring might have undergone during the relevant time period. Therefore, the brightness changes quoted in this paper for compact radio knots (computed subsequent to normalization) actually represent *relative* changes—changes *relative* to the flux in the diffuse ring, which itself appears to be undergoing secular fading. This is an important distinction, and it will be reiterated throughout this paper.

3.4. *Measurement of Fractional Brightness Changes and Proper Motions*

To measure the positional shifts and relative fractional brightness changes of radio knots in Cas A, we have adopted the least-squares technique used by Tuffs (1986) in his two-epoch comparison, reviewed briefly here. This algorithm is powerful in that it minimizes the effects of variations in the large-scale background reconstruction between epochs resulting from varying aperture coverage. It also facilitates the separation of the flux in a knot from that of the background.

Given a reference image B_{ij} and a comparison image A_{ij}, we first selected a small region around each knot in our sample. The size and position of a given region was chosen such that it contained the knot of interest at all epochs and isolated it, as best as is possible, from other small-scale emission structure in its vicinity. Within this region we then minimized the quantity

$$T(\xi) = \sum_{i=1}^{I} \sum_{j=1}^{J} Q_{ij}^2(\xi) , \quad (1)$$

where

$$Q_{ij}(\xi) = B_{ij} - SA_{ij}(\Delta\alpha, \Delta\delta) - iGX - jGY - H , \quad (2)$$

with respect to the 6-vector $\xi = (\Delta\alpha, \Delta\delta, S, GX, GY, H)$. Here, $(\Delta\alpha, \Delta\delta)$ represents the shift in right ascension and declination of map A_{ij} relative to map B_{ij}, S is the scale change in knot brightness between epochs, GX and GY are differences in background slope between the two images, and H absorbs a difference in constant offset. The summation is performed over all pixels in the selected region. Best-fit values for ξ were obtained through a least squares multiparameter minimization procedure. This procedure was executed five times for each knot, cycling through the five epochs of comparison images (1978, 1982, 1983, 1985, and 1990)—in each case the epoch 1987 map was used as the reference image, B_{ij}.

Uncertainties in $\Delta\alpha$, $\Delta\delta$, and S were determined with the variational χ^2 method described by Avni (1976) and Tuffs (1986), assuming 3 d.o.f. Additional discussion is provided by Anderson (1993).

3.5. *Peak Brightness Estimates*

The technique described in the previous section is sensitive only to *scale* changes in brightness; the actual brightness of each knot is not obtained through this method. An estimate of the fiducial 1987 intensity of each knot, measured above the local background level, has been obtained from an image in which large-scale structure has been spatially filtered from the remnant. Approximate high-pass filtering was accomplished by convolving the 1".3 C-band image to 10" (roughly the width of the narrow component of the bright ring) and subtracting it from the original image. A brightness estimate was then extracted by fitting a two-dimensional Gaussian to the peak intensities associated with each compact feature. While larger features tend to be somewhat oversubtracted by this method, the *ranking* of brightnesses among knots is more or less accurate. Only one feature resulted in a negative intensity; in this case an estimate was obtained by eye for the height of the knot above the local background.

The resultant spatially filtered brightness distribution is shown in Figure 3 (Plate 9). Most maxima in this image were included in our knot sample, so Figure 3 gives an idea of the spatial distribution and morphological appearance of the knots studied here. Note that the diffuse plateau contains a considerable amount of fine-scale structure—much more than is evident in the full spatial-synthesis image in Figure 1.

This image also shows other compact structures which are *not* studied here. Most prevalent are the honeycomb-like filamentary cells which span the remnant's surface. Filaments in the western hemisphere of the remnant tend to be brighter and sharper than those found in the east.

3.6. *Results of Multi-Epoch Fits*

For each knot, weighted linear fits were computed for $(\Delta\alpha, \Delta\delta)$ as a function of time to determine a best-fit proper motion. Positional fits with errors greater than ± 1 pixel (0".4) were not included in the velocity computations, thus some proper motions are based on less than 6 epochs of data. The resultant uncertainties in these proper motions correspondingly reflect the lesser amount of data. Weighted fits to the brightness scaling factors were also performed to obtain the fractional change in brightness relative to the large-scale ring emission ($\Delta B/B$) experienced by each knot over this time period.

The nominal data for each VLA image used in these fits (epochs 1983–1990) was taken to be that of the corresponding B-configuration observation—the configuration in which the

PLATE 9

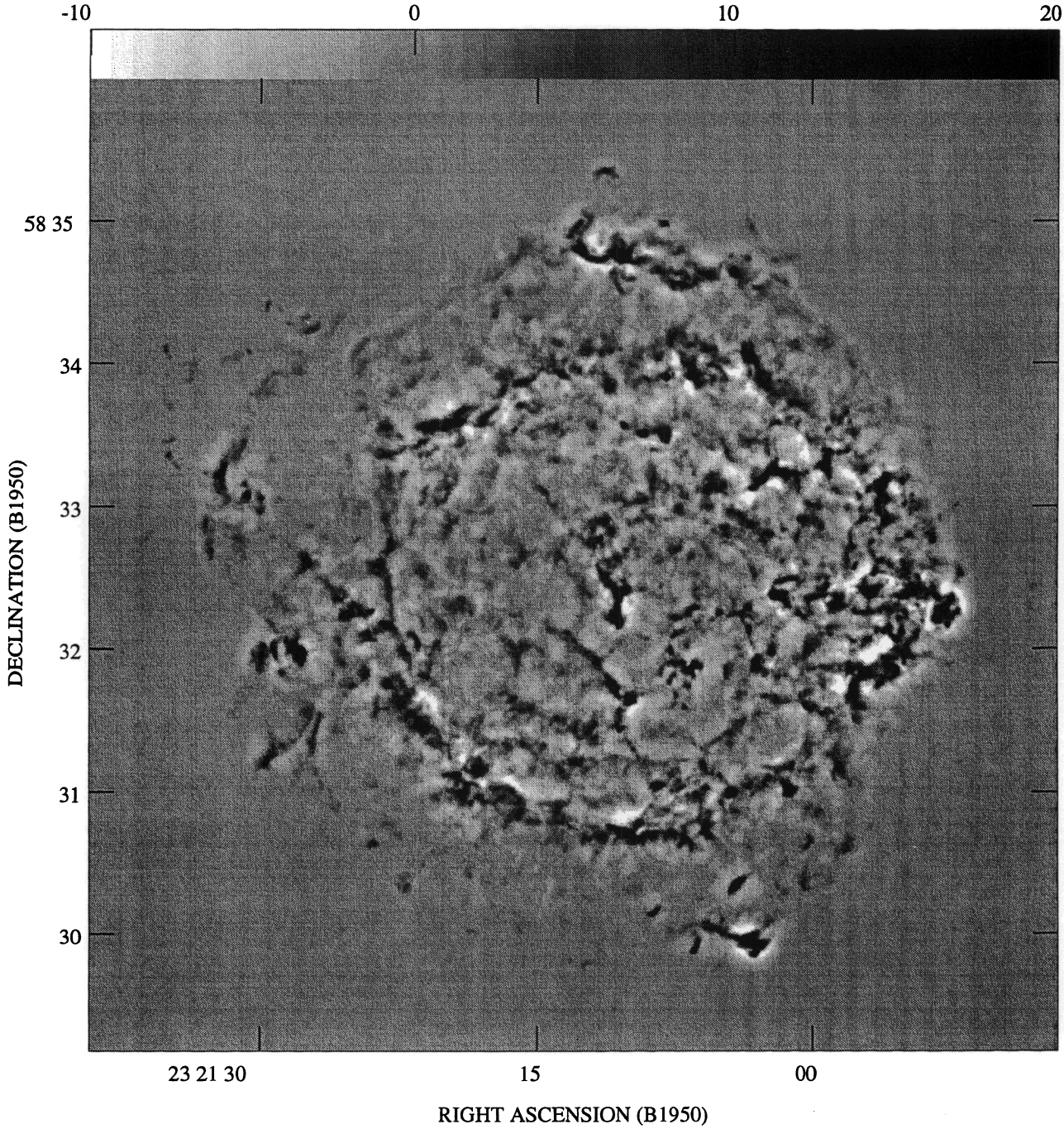

FIG. 3.—A spatially filtered $\lambda = 6$ cm image of Cas A, epoch 1987. Spatial structure on scales $> 10''$ has been removed. Gray-scale is in units of mJy beam^{-1}.

ANDERSON & RUDNICK (see 441, 316)

most visibilities were acquired. The average observing date for the 5 km Telescope data has been adopted for the 1978 and 1982 observations. The addition of an uncertainty term describing the spread in dates over which data for a given epoch were collected does not affect the uncertainties quoted below.

The results of these fits are tabulated in Table 3 and are listed in the tables notes.

4. THE TEMPORAL EVOLUTION OF COMPACT RADIO EMISSION FEATURES IN CASSIOPEIA A

Here we explore the results of the multi-epoch measurements of proper motions and brightness changes associated with compact features in Cas A discussed in § 3 and tabulated in Table 3. Of particlar interest is the question of whether or not the radio-emitting material in Cas A has been strongly decelerated, as this has bearing on limits for current magnetic field amplification and turbulent particle acceleration in the remnant. We also look at the spatial distribution of brightness changes among compact radio features in the remnant. A summary of these findings is provided in § 6. In § 7 we show how these results support a picture of deceleration-powered emission from clumpy ejecta.

4.1. *Proper Motions of Radio Knots*

Figure 4 shows the spatial distribution of proper motion vectors derived for the 304 knots in our sample. A plot of vectors describing the differences between proper motion vectors displayed here and those measured by Tuffs (1986) reveals no striking systematic differences between these two studies. However, a comparison of Figure 4 with the plot of proper motion vectors derived by Tuffs (1986) clearly indicates the advantage of averaging positional data over several epochs. A significant fraction (18%) of the tangential component of motion measured by Tuffs has been eliminated in the averaging. We are also aided by a significant improvement in image quality obtainable with the VLA.

To deduce an overall expansion age appropriate for the radio knots in Cas A, we must assume a model for the observed knot proper motions. The simplest model is one of linear expansion: proper motions are related linearly to the (projected) distance from the expansion center. This corresponds to either of the following scenarios: (1) all knots were ejected with the same initial velocity and have suffered the same amount of deceleration, or (2) no deceleration has occurred, but a range of initial velocities is allowed.

The proper motion vectors in Figure 4 have been fit with a linear expansion model to derive a radio expansion center and timescale. Figure 5 shows the results of weighted linear fits to the right ascension and declination components of proper motion. The resulting timescales are virtually equivalent in right ascension and declination, with $T_{RA} = 866 \pm 8$ yr, and $T_{Decl.} = 861 \pm 9$ yr. This is in contrast to the results of Tuffs, who found a significantly longer timescale in right ascension

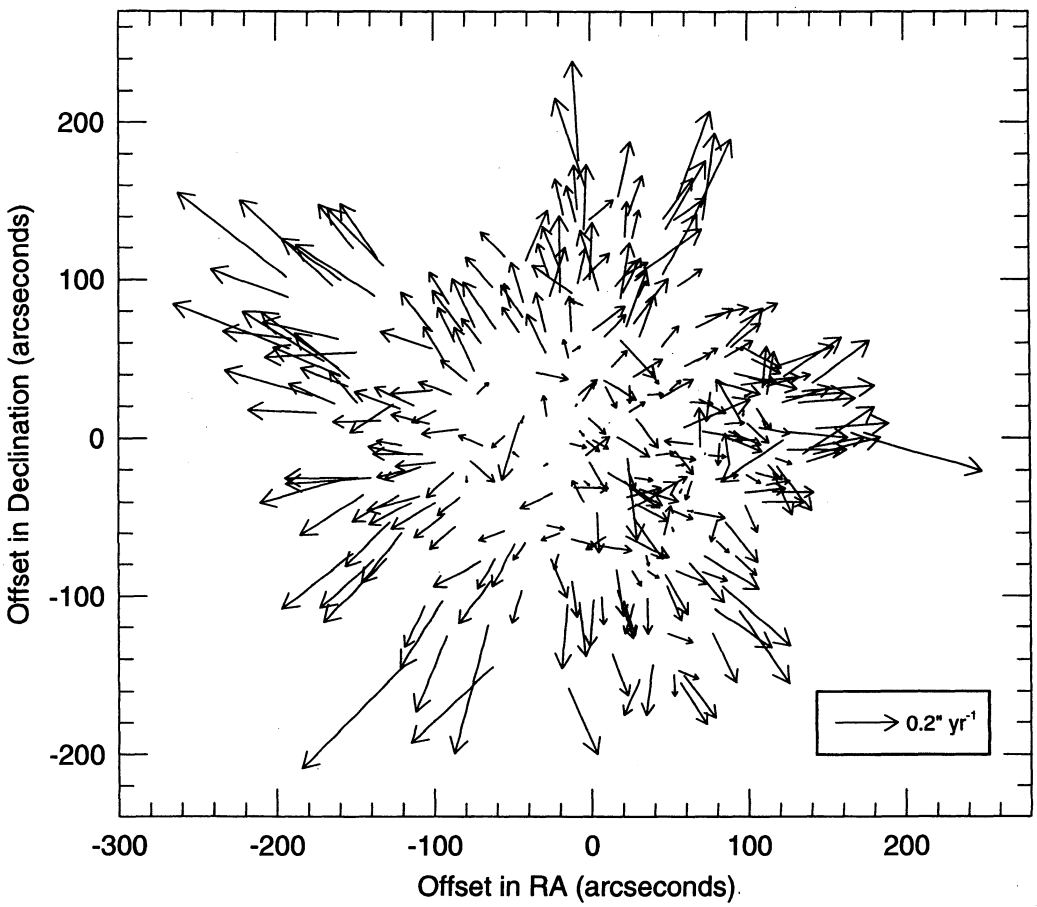

FIG. 4.—Proper motion vectors derived for 304 compact radio features in Cas A from 6 epoch linear positional fits. Position offsets are measured with respect to the radio knot expansion center.

than in declination. It should be noted, however, that our knot sample includes several fast-moving, rapidly brightening features in the northeast jet region which were too faint to be included in Tuffs' sample. The expansion center derived from our data is $\alpha(1950) = 23^h21^m10^s.3 \pm 0^s.2$, $\delta(1950) = +58°32'25''.6 \pm 3''.1$, and is marginally compatible, within the quoted errors, with the measurement by Tuffs. This position is offset from the optical expansion center by $24'' \pm 3''$ to the west and $8'' \pm 3''$ to the north.

It is clear from Figure 5 that some knots are not well fitted with a linear model—particularly the group of knots lying to the west (positive offset), beneath the best-fit line in right ascension. These slow-moving knots are influencing the fit toward longer expansion timescales in the east-west direction. The deviant western knots become especially obvious in a plot of vector residuals from the linear model (Fig. 6). The significantly nonradial motions evident in the western part of the remnant clearly indicate the presence of some type of perturbing agent active in this region. Keohane et al. (1995) discuss additional indirect evidence for such a cloud.

Also evident in Figure 6 are a number of knots lying outside the main radio shell with radial proper motions much higher than those derived for an overall linear fit to the remnant's expansion. This high-velocity component can be seen in a plot of radial proper motion versus projected radius, both measured with respect to our derived expansion center (Fig. 7). Beyond a radius of $\sim 120''$ there is a significant increase in the slope of this relation, indicating a transition between expansion timescales. Several of these fast-moving features lie in the "jet" region to the northeast, having velocities of up to 6000 km s^{-1}. These large proper motions are undoubtedly related to the anomalously high velocities associated with the optical knots observed in the jet.

The nonlinearity of the distribution in Figure 7 can be understood in terms of concentric "shells" of radio knots which have undergone varying degrees of deceleration. The

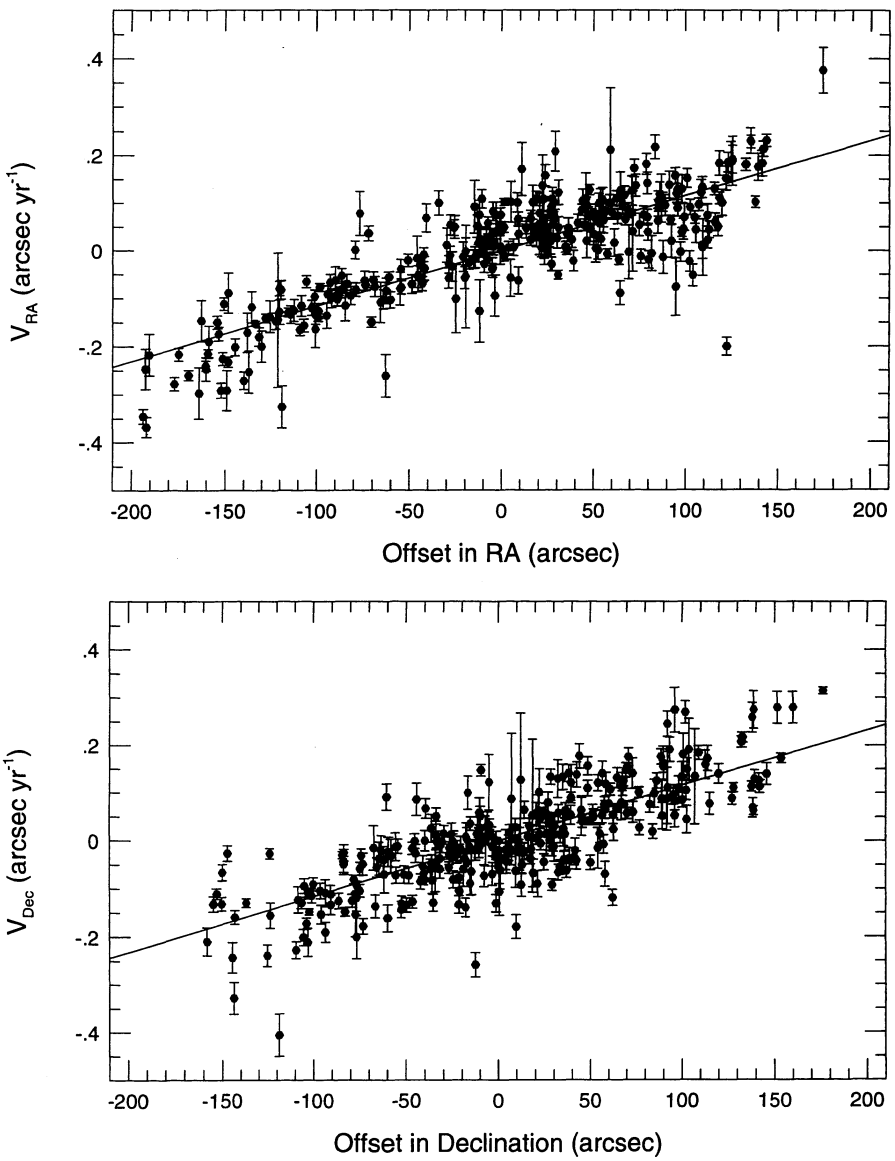

FIG. 5.—Linear weighted fits to the right ascension and declination components of proper motion as a function of position within the remnant

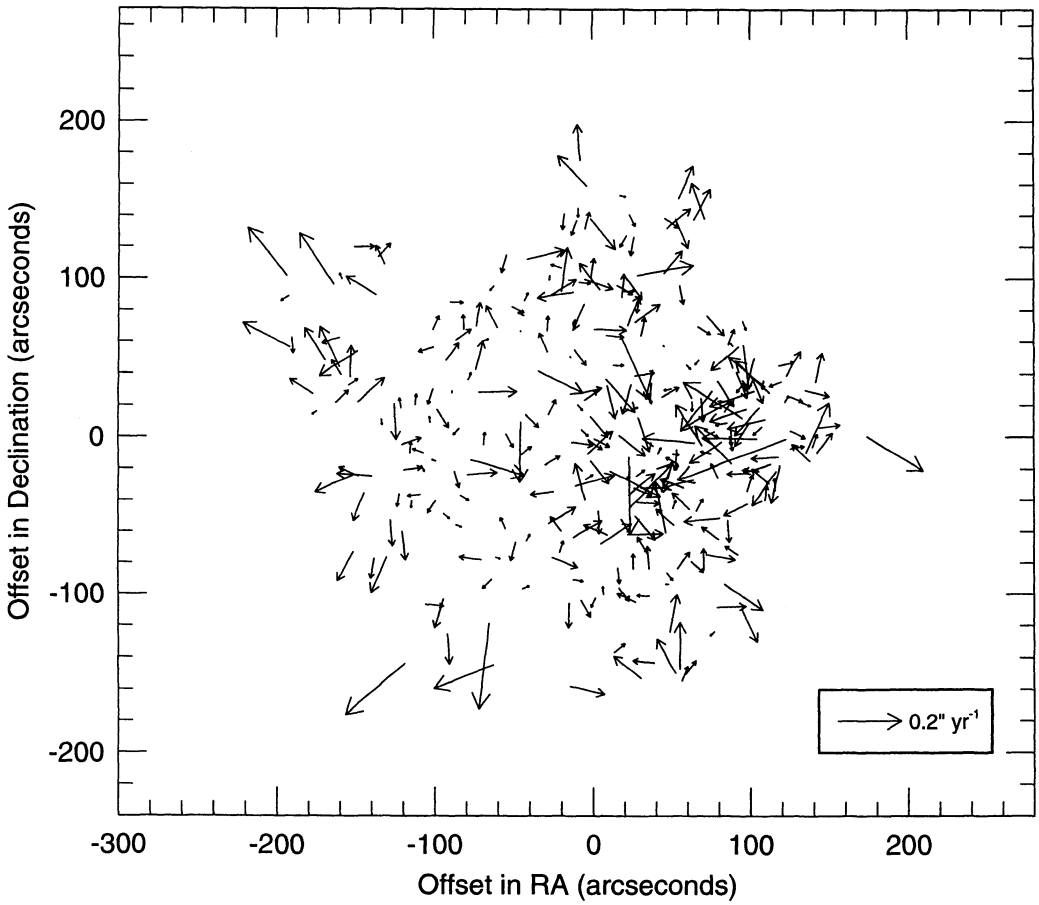

FIG. 6.—Residual velocity vectors representing the vector difference between knot proper motions and a linear expansion model

knots in the region of the main radio shell, at radius 100″, have been most severely decelerated and exhibit an expansion age of ~940 yr. Shells of knots outside the radio ring show decreasing deceleration with radius and have expansion ages between 900 and 550 yr. The degree of curvature apparent in Figure 7 thus reflects the contrast in deceleration experienced by the inner and outer knots.

4.2. *Azimuthal Variations in the Expansion Timescales of Radio Knots*

Given the spatially coherent deviations from linear expansion evident in Figure 6, it is important to investigate expansion timescales for regional subsets of knots, as well as for the system as a whole. To this end, the remnant has been divided

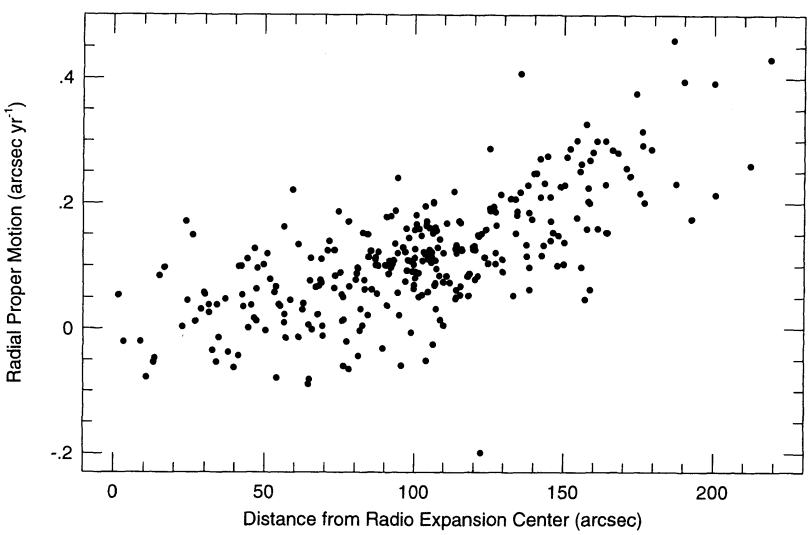

FIG. 7.—Radial component of proper motion plotted vs. distance from the radio expansion center

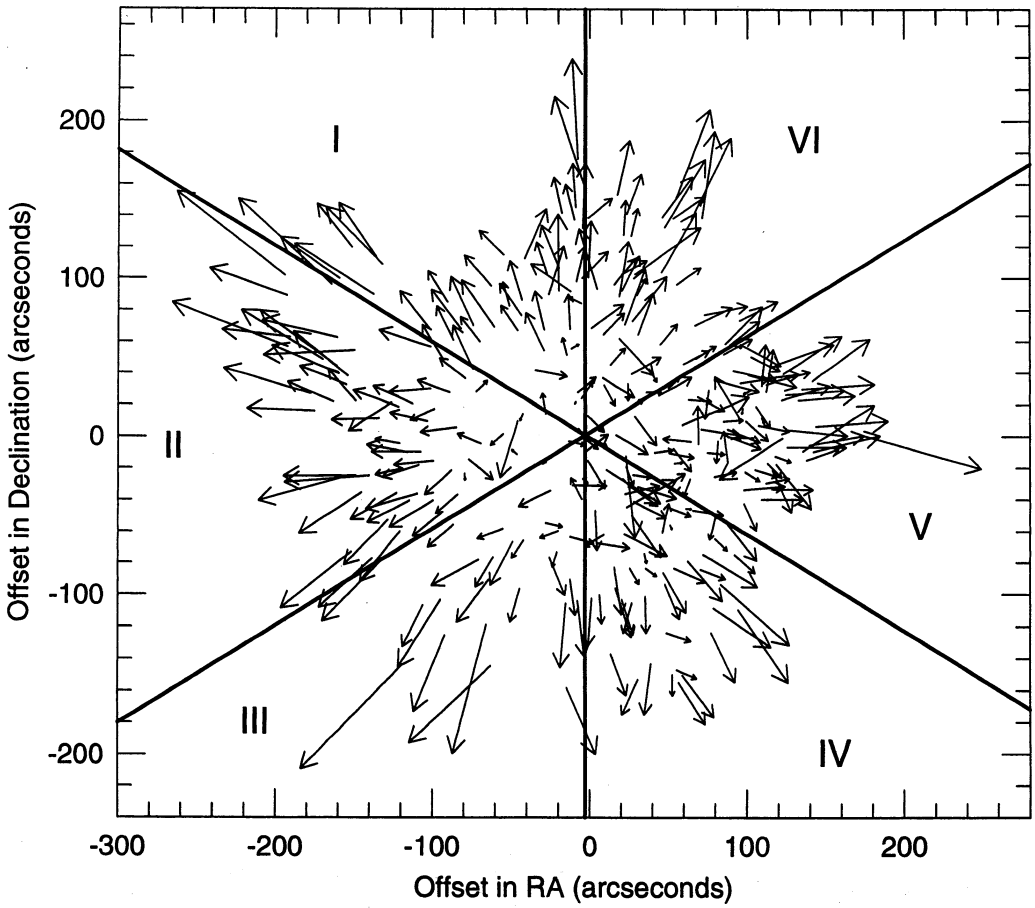

FIG. 8.—Sectors defining regions for local expansion timescale calculations

into six equal sectors about the radio expansion center, as displayed in Figure 8 (labeled sectors I–VI).

To compute expansion timescales in individual sectors, the observed proper motion vectors have been projected onto a line bisecting the relevant sector. Distances from the remnant center are computed in this way as well. The resulting expansion center for a given sector will then lie somewhere along the bisector, at positive radii (within the wedge) or at negative radii (in the opposite wedge), depending on the peculiarities of the velocity distribution. Figure 9 shows the radial distribution of proper motions computed for the configuration of sectors shown in Figure 8. The results of the timescale computations are tabulated in Table 4.

Timescales of ~500–700 yr are derived for all sectors with the exclusion of sector IV (corresponding to the sourthwest corner of the remnant), where a timescale of 2100 yr is measured. The shortest timescales (~500 yr) are found in the eastern half of the remnant, particularly in the southeast. It should be noted that the timescales derived in sectors are somewhat dependent on the choice of sector center, with variations commensurate with the quoted errors.

The nonradial motions in the west manifest themselves as a marked broadening of the distribution of proper motions as a function of distance. Sector V in Figure 9 is certainly not well modeled by linear expansion, thus the timescale derived here is not physically meaningful. However, there is an upper

TABLE 4

EXPANSION TIMESCALES IN AZIMUTHAL SECTORS

	ALL KNOTS			BRIGHT KNOTS			FAINT KNOTS		
SECTOR	N	T (yr)	R_c	N	T (yr)	R_c	N	T (yr)	R_c
I.....	47	630 ± 20	22″ ± 4″	19	620 ± 30	20″ ± 4″	28	610 ± 40	29″ ± 7″
II.....	60	520 ± 10	43 ± 3	20	540 ± 20	40 ± 6	40	520 ± 20	45 ± 4
III.....	31	480 ± 20	39 ± 5	10	450 ± 30	43 ± 7	21	520 ± 40	33 ± 8
IV.....	53	2100 ± 360	−110 ± 20	32	7000 ± 3200	−590 ± 270	21	440 ± 30	40 ± 6
V.....	67	660 ± 30	46 ± 6	44	630 ± 40	55 ± 6	23	780 ± 90	2 ± 10
VI.....	46	730 ± 40	13 ± 5	27	800 ± 70	8 ± 7	19	650 ± 50	18 ± 7

NOTES.—Expansion timescales (T) and centers (R_c) computed for knots in azimuthal sectors in Cas A. Timescales are computed for the entire knot sample and for bright and faint knot subsets. N indicates the number of knots in each sector.

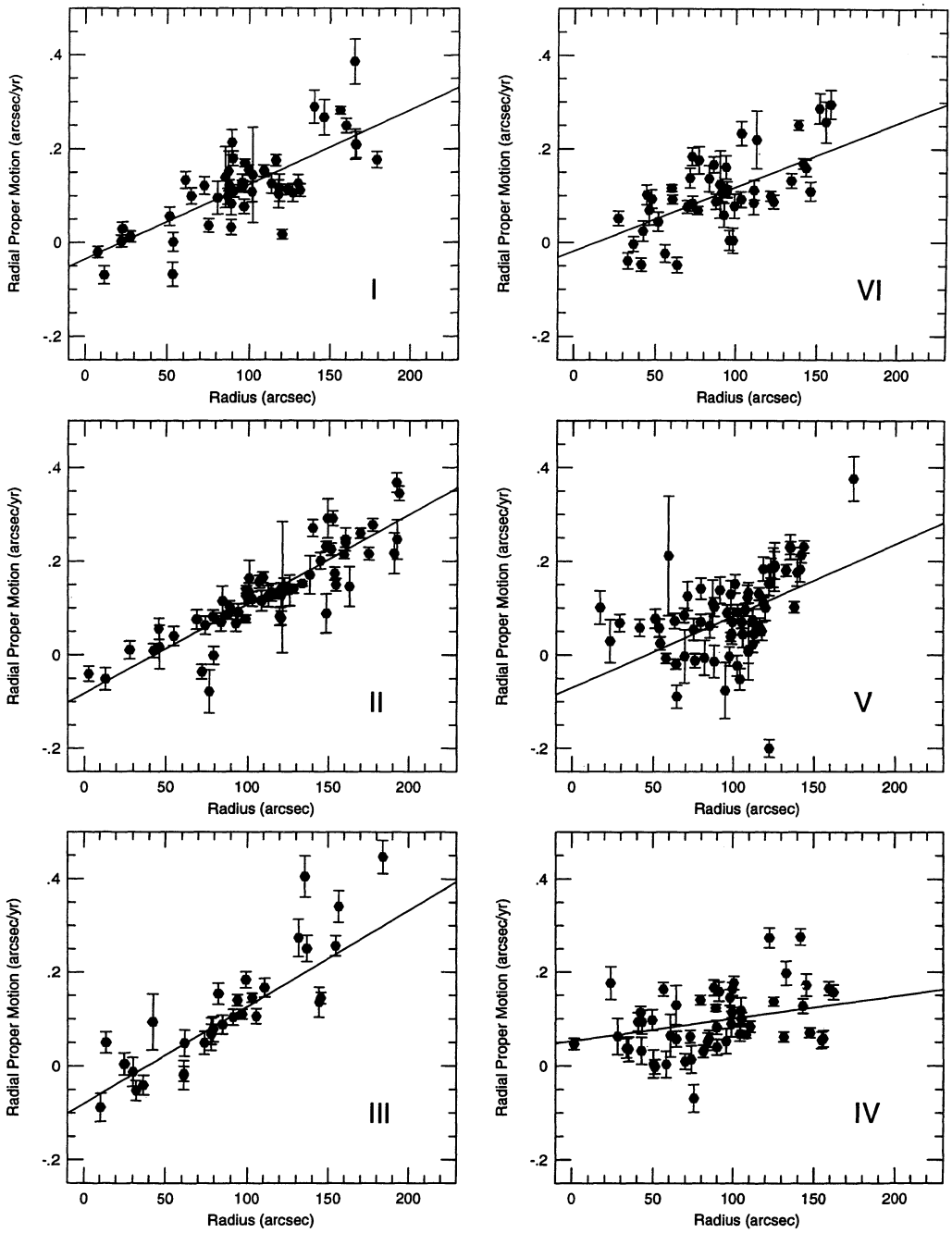

FIG. 9.—Radial proper motion vs. projected radius for knots in sectors demarcated in Fig. 8. Lines indicate error-weighted linear fits to the distributions.

envelope of knots in sector V which appears to be expanding more or less normally, thus the associated timescales are similar to other sectors despite the disordered motion.

The fact that linear fits in most sectors yield a positive offset in radius (R_c, in Table 4) reflects the positive curvature in V_r versus R found for the system as a whole. As we have not forced a common origin for these fits, and they are not constrained by knots on both sides of the remnant, this curvature biases the fits toward shorter timescales. Nevertheless, comparisons of sector timescales derived in this way do yield valid information concerning azimuthal variations in deceleration around the remnant.

4.3. *Expansion Timescale–Knot Brightness–Radius Correlations*

If the knot sample is divided into two subsets, those brighter and fainter than the median brightness (12.2 mJy beam^{-1}), a very different picture of the expansion is obtained. As a caveat we note that the faint knots are not a homogeneous population—some of them are distinct isolated features; others, especially interior to the bright ring, are likely to be superpositions of very faint filamentary structures. With this in mind, we find that for bright knots, the expansion timescale in right Ascension is 914 ± 12 yr, and in declination, 907 ± 12 yr,

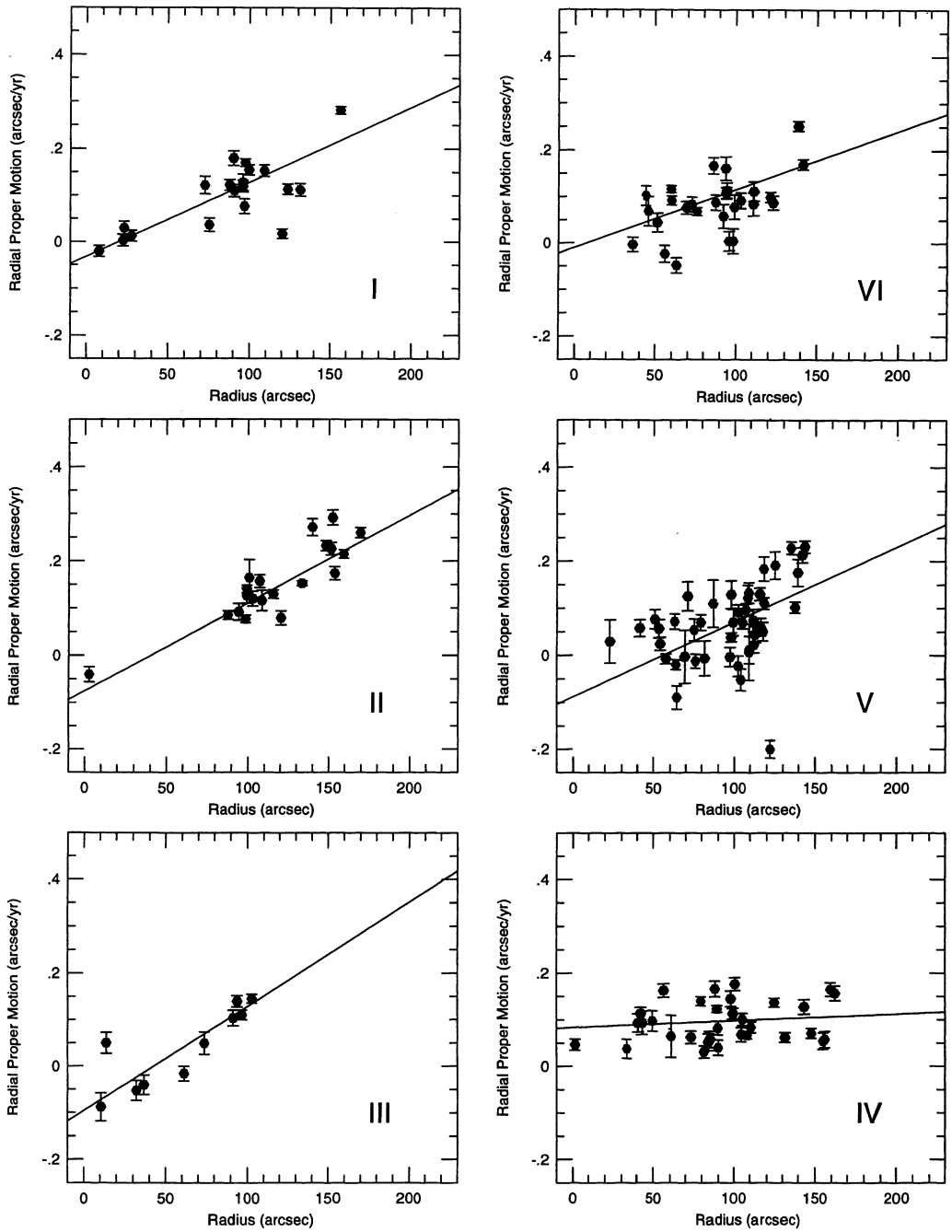

FIG. 10*a*

FIG. 10.—Radial proper motion vs. projected radius for knots in sectors demarcated in Fig. 8 for (*a*) knots brighter and (*b*) knots fainter than the median knot brightness of 12.2 mJy beam^{-1}.

while for faint knots, ages of $T_{RA} = 758 \pm 11$ yr and $T_{Decl.} = 736 \pm 14$ yr are obtained. The expansion of these two knot subsets defines different centers as well: the center for faint knots is displaced 31".5 west and 8".7 north of the center of bright knot expansion. The difference between the faint and bright knot samples is dominated by those in the west. The expansion timescales associated with the eastern half of the remnant are comparable between bright and faint knots: $T_{RA} = 600 \pm 21$ (590 $\pm$ 18) years and $T_{Decl.} = 628 \pm 16$ (653 $\pm$ 17) yr for bright (faint) knots.

Figures 10*a*–10*b* show the distributions of radial proper motion with radius for bright and faint subsets of knots separated into the 6 azimuthal sectors defined in Figure 8. The timescales and expansion centers derived for each sector for bright and faint knot subsamples are listed in Table 4. Faint knots show a considerably more uniform expansion than do bright knots. It is clear that the long timescales derived for the southwestern part of the remnant are entirely due to bright features; the faint features there expand as fast as the rest of the remnant.

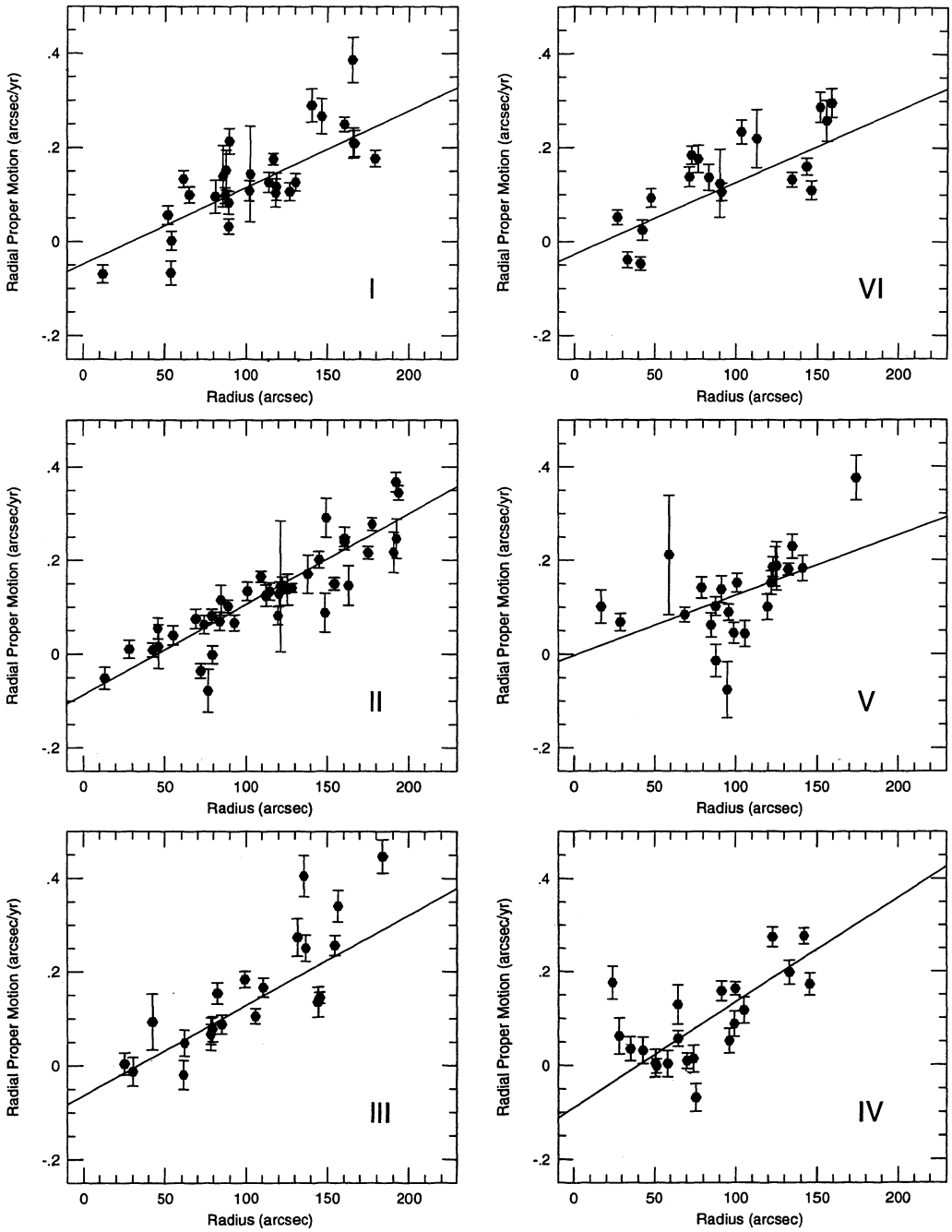

FIG. 10*b*

Tuffs (1986) noted a dependence of expansion timescale ($T = R/V_r$, computed for each knot individually) on feature brightness and radial position (R); these trends are considerably stronger in our data. Significant correlations have been confirmed with the Spearman rank correlation test, applied to the database as a whole and to subsets of knots segregated in various ways to identify secondary regulating factors. The results of these tests are listed in Table 5. (One highly deviant inner knot, with expansion timescale <330 yr, has been excluded from these tests and from the plots presented in this section.)

For all significant correlations using the various subgroups of knots, *expansion timescale decreases with radius and increases with knot brightness*. We find, however, no significant direct correlation between knot brightness and radius. We discuss here the subgroupings which give the strongest correlations.

Inverse expansion timescale is most strongly correlated with brightness for knots outside the ring (see Fig. 11). Bright knots in the plateau region expand with an average timescale of 930 yr, while faint plateau knots have an average timescale of 740 yr. Compact features inside the ring show no significant correlation between timescale and brightness.

The brightening knot subset also shows a signficant rank correlation between brightness and inverse timescale. In addition, significant brightness-timescale correlations are found for

TABLE 5

RESULTS OF SPEARMAN RANK CORRELATION TEST

SUBSET	NUMBER OF KNOTS	$1/T$ VERSUS B		$1/T$ VERSUS R	
		R_s	$P(R_s)$	R_s	$P(R_s)$
All knots	303	−0.22	0.12×10^{-3}	0.23	0.63×10^{-4}
Faint knots	152	−0.22	0.54×10^{-3}	0.34	0.20×10^{-4}
Bright knots	151	−0.08	$0.35 \times 10^{+0}$	0.08	$0.36 \times 10^{+0}$
Fading knots	99	−0.10	$0.34 \times 10^{+0}$	0.21	0.37×10^{-1}
Brightening knots	204	−0.27	0.96×10^{-4}	0.24	0.43×10^{-3}
Inner knots	138	−0.07	$0.43 \times 10^{+0}$	0.08	$0.35 \times 10^{+0}$
Outer knots	165	−0.37	0.89×10^{-6}	0.28	0.24×10^{-3}
Eastern knots	122	0.00	$0.97 \times 10^{+0}$	0.43	0.95×10^{-6}
Western knots	180	−0.27	0.23×10^{-3}	0.06	$0.43 \times 10^{+0}$

NOTES.—Results of a Spearman rank test for correlations between inverse expansion timescale, radius and brightness. R_s is the rank coefficient of correlation, and $P(R_s)$ is the two-tailed probability that the given distribution satisfies the null hypothesis (see, e.g., Press et al. 1992). The cutoff between bright/faint knots is 12.2 mJy beam^{-1} and between inner/outer knots, a radius of 100″.

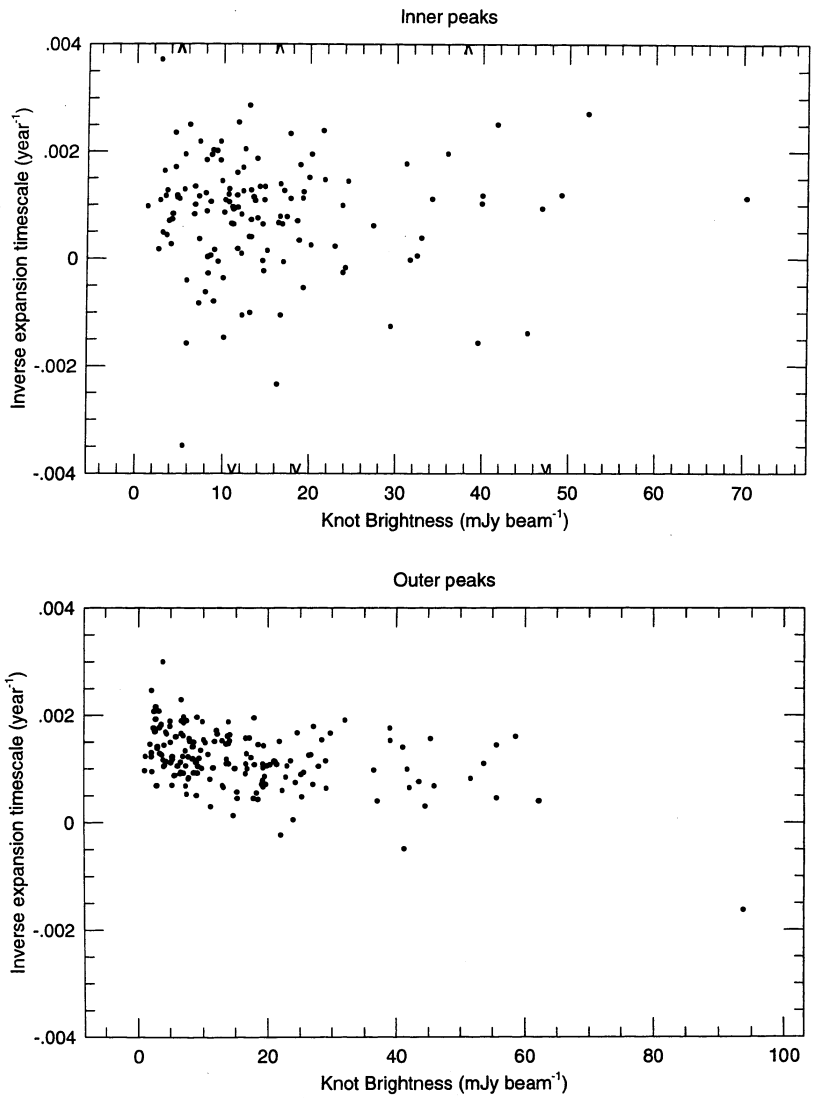

FIG. 11.—Inverse expansion timescale vs. knot brightness for knots inside and outside the radio ring. Carats along plot edges indicate the positions of a few knots which fall outside of the vertical plot range.

knots in the western half of the remnant (but not in the east) and for faint knots (but not for bright).

In comparing inverse timescales with radial position within the remnant, the strongest correlation is found for knots in the eastern hemisphere. Western knots do not show a correlation. Segregating the knots by brightness reveals a significant correlation between radius and inverse timescale for faint knots, but not for bright knots. The radius-timescale correlation also exists at a highly significant level for knots outside the ring and for knots which are brightening relative to the ring emission. We see now that the nonlinearity of radial proper motion (and thus $1/T$) as a function of projected radius evident in Figure 7 is due mostly to fast faint knots in the eastern plateau region.

In summary, *there appear to be at least two different kinematic populations of compact radio features in Cas A*. The brightness of a knot and its position within the remnant (inside or outside of the ring) are related to its velocity.

4.4. *Knot Accelerations*

Given that significant deceleration has already occurred among compact radio features in Cas A, we have tested the positional data derived in this study for discernible second-order time dependencies. The data were fitted to functions of the form $z = z_0 + v_{0_z} t + a_z t^2$ (where z is the knot position in right ascension or declination) to place limits on possible accelerating and/or decelerating motions. These fits were weighted by the positional uncertainties ascertained for each epoch; the errors in the coefficient a_z were similarly weighted. Uncertainties in a_z due to the several month timespan over which data for a given epoch were acquired were negligible in comparison.

For individual knots, the derived accelerations were generally less than the associated errors. Most significant detections of knot deceleration appear to be caused by changes in the structure of the feature or confusion with other emission.

Taken as a whole, the measured acceleration field appears somewhat disordered but it is not consistent with random noise. Error-weighted vector sums, computed in the right ascension, declination, and radial coordinates, yield net acceleration components

$$a_{\mathrm{RA_{net}}} = 1.6 \pm 0.6 \text{ mas yr}^{-2}, \quad a_{\mathrm{Decl_{net}}} = 6.3 \pm 0.6 \text{ mas yr}^{-2},$$
$$a_{r_{\mathrm{net}}} = 2.0 \pm 0.6 \text{ mas yr}^{-2}.$$

For comparison, even if the knots were decelerating at a constant rate since their ejection, we would expect to see a systematic (negative) radial acceleration of ~ 1.4 mas yr^{-2}.

We have tested these net accelerations for a systematic origin (e.g., due to a relative positional image shift in one epoch) by recomputing the second-order fits 6 times, sequentially excluding each epoch from the determination. The component $a_{\mathrm{Decl_{net}}}$ maintains a level of 10 σ significance in each case, while $a_{\mathrm{RA_{net}}}$ and $a_{r_{\mathrm{net}}}$ vary in significance between 0.5 and 2 σ. *The net northern acceleration therefore cannot be due to a systematic bias imposed by a single epoch.* The possibility remains, however, that the acceleration component $a_{\mathrm{Decl_{net}}}$ may be due to a systematic bias involving more than 1 epoch.

We conclude that a net radial *deceleration* among compact features in Cas A is not observed over the 12 yr time period encompassed by the radio image archive. This is a bit surprising, but further examination of possible systematic effects will have to be investigated to put the result on a firm foundation. We do find statistical evidence for a net *acceleration* toward the north. We note that further evidence supporting the existence of a northward-directed force at work in Cas A is provided by the proper motions of the optical quasi-stationary flocculi (QSFs; see van den Bergh & Kamper 1985). Based on their dynamics and chemical composition, these optical knots are thought to comprise dense clouds of circumstellar material shocked in the passage of the SNR blastwave. Although distributed across the front face of the remnant, few QSFs exhibit a significant southward component of proper motion.

4.5. *Evolution of Synchrotron Brightness in Radio Knots*

The measurement of brighness changes for compact features in Cas A is complicated by calibration uncertainties for this very strong source as well as other factors such as inadequate resolution and sensitivity to large-scale structure (Dickel & Greisen 1979) and the use of Stokes parameters I–Q (Tuffs 1986). In the current work, we have normalized the large-scale flux distribution to be the same at all epochs (with an uncertainty of $\approx 1\%$ at each epoch), as described above. We then find most compact features brightening relative to the bright radio ring, with a mean (and median) brightness increase of $+1.6\%$ yr^{-1} over a 12 yr baseline. Two-thirds of the features show brightnes changes relative to the ring in the range -2.2% yr^{-1} to $+5.2\%$ yr^{-1}. Since total flux measurements for the whole remnant show a decrease of $\approx 1\%$ yr^{-1}, the mean brightness change on an absolute scale is quite small, although individual features show much larger variations in both directions.

The spatial distribution of relative fractional changes in brightness derived for our knot sample is displayed in Figure 12. This spatial distribution is similar to that seen in a simple difference image between two epochs. A band of rapidly brightening knots is found in the southwest quadrant of the remnant. Brightening knots are also prevalent in the jet region and southeastern plateau. These are primarily responsible for the overall increase in the rate of fractional brightening with distance from the remnant center beyond a radius of $\sim 130''$ (Fig. 13).

The rate of fractional brightening increases with distance from the remnant center. Upon further analysis, it becomes clear that this trend is due primarily to faint peaks outside the shell in the eastern half of the remnant.

If we assume for simplicity that the characteristic knot brightening/fading curve is exponential, e-folding lifetimes can be obtained by inverting the fractional brightness change measurements. These radiative lifetimes are histogramed in Figure 14. A characteristic lifetime for both brightening and fading knots is on the order of 25–30 years, similar to the lifetimes for optical knots found by Kamper & van den Bergh (1976).

There is a weak but significant tendency for brighter knots to brighten more rapidly than fainter knots. This trend is expressed in the histograms in Figure 15, where the knots have been separated into two groups at a cutoff brightness of 20 mJy beam^{-1} (chosen to maximize the difference between the two populations). Application of the Kolmogorov-Smirnov test indicates that these distributions are different at a significance level of 97%. The offset between these two distributions suggests that the characteristic knot brightening curve is slightly convex—that the rate of brightening increases with time. In addition, the fact that frequency distribution of brightness change for all knots is skewed toward brightening suggests a light curve in which knots typically brighten more slowly than

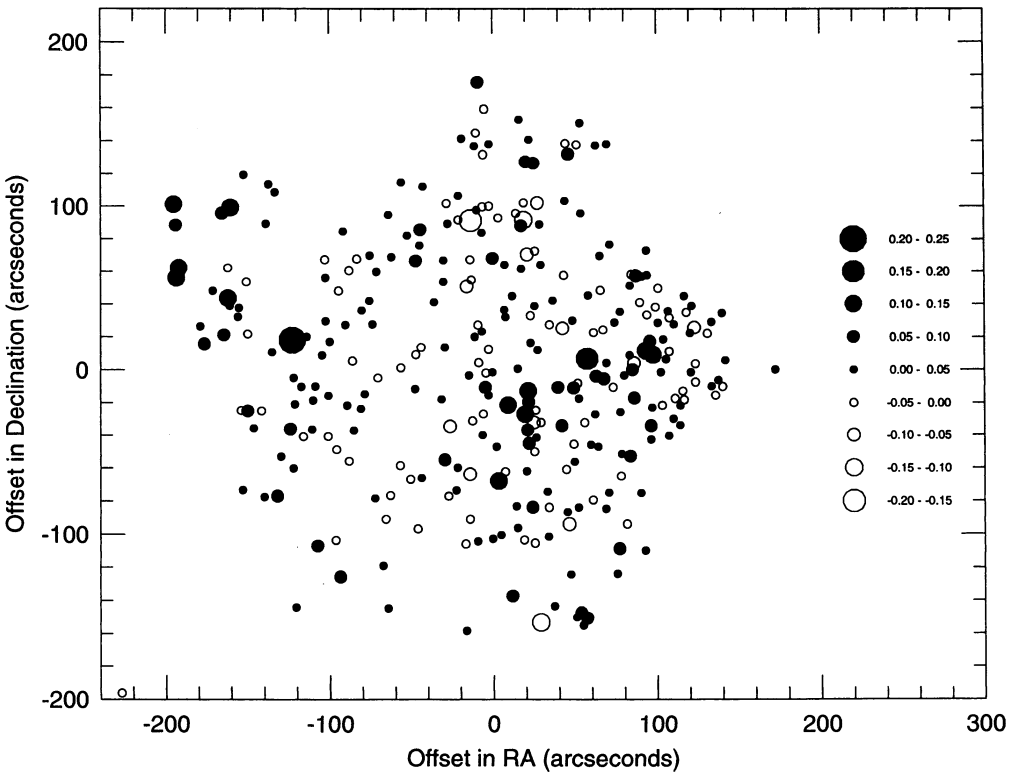

FIG. 12.—Fractional brightness changes relative to the fading ring, for compact features in the knot sample

they fade, thus enhancing the probability of finding them in a brightening phase.

5. BULK EVOLUTION OF THE LARGE-SCALE RADIO RING

Given the wide range in expansion timescales obtained using different subsets of radio knots, it appears difficult to specify one timescale that will characterize the overall expansion of the radio-emitting material. Furthermore, as pointed out by Green (1988), it is not clear that the expansion traced out by compact features is necessarily indicative of the dynamics of the bulk ejecta. Due to the wide variations in expansion velocity and brightness change measured in the map plane, we turn, as did Green (1988), to an examination of secular changes in the visibility plane to isolate large-scale motions. The *u-v* distribution on short baselines is dominated by the Fourier transform of the bright radio ring (see Fig. 16). A uniform *expansion* of the ring in the map plane will yield a *contraction* of all short-baseline features in the *u-v* plane.

We compared the 1985 and 1990 *u-v* distributions at $\lambda = 20$ cm by first gridding the visibility amplitudes into *u-v* cells of area 30×30 kλ. Following the method of Green (1988), the 1990 data were gridded into cells of systematically decreasing size: 0.05% smaller, 0.10% smaller, etc. The gridded 1985 *u-v*

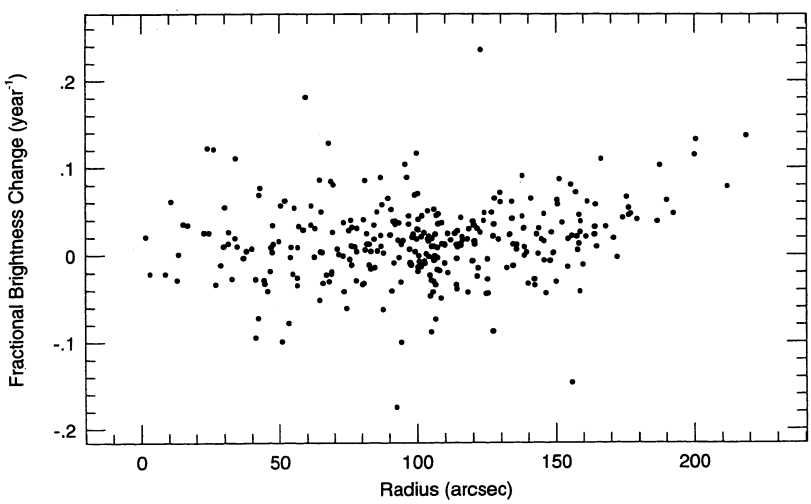

FIG. 13.—Annual fractional change in radio knot brightness as a function of distance from the radio expansion center

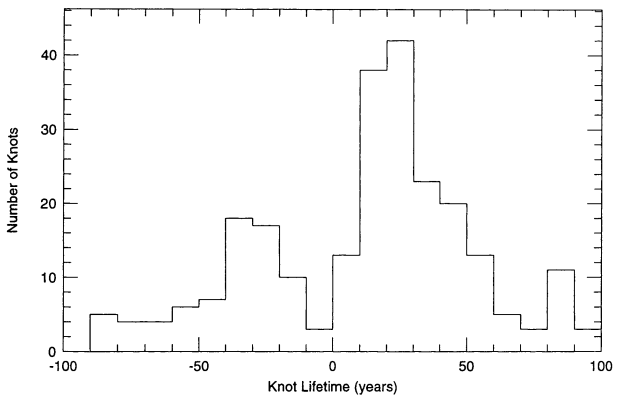

FIG. 14.—Histogram of radio knot *e*-folding lifetimes. A limited range of −100 to 100 yr is plotted.

data were then combined with the 1990 data for each choice of cell size, *i*, to form the statistic

$$U(i) = [UV_{1985} - S_{\rm bulk}(i) * UV_{1990}(i)] , \quad (3)$$

where UV_{1985} is the gridded *u-v* amplitude for epoch 1985, and $UV_{1990}(i)$ is the *u-v* amplitude for epoch 1990 in the rescaled grid. The factor $S_{\rm bulk}(i)$ allows for secular changes in brightness in the bulk radio ring and differences in absolute calibration between epochs. The statistic U was then minimized in summation over all *u-v* cells to obtain the best-fit contraction rate, F, and visibility amplitude scaling factor, $S_{\rm bulk}$. This procedure differs from that used by Green (1988), who minimized the statistic $|1 - UV_1/UV_2|$—a method much more sensitive to noise in low-level regions of the *u-v* plane. Errors were determined by the variational method of Avni (1976), allowing 2 d.o.f. ($S_{\rm bulk}$ and 1990 cell size).

The comparisons were limited to amplitudes on baselines smaller than 3 kλ (just beyond the third minimum in the ring's Bessel function) to eliminate possible contributions from small-scale features. Visibilities on baselines shorter than 0.5 kλ were excluded due to potential corruption by the van Vleck bias (van Vleck & Middleton 1966). Most of the central maximum in the *u-v* plane was also excluded to assure that the large amplitudes there did not strongly influence the minimization. Only enough short baseline data were retained to clearly define the first minimum at all *u-v* position angles, resulting in a lower *u-v* limit of 0.5–0.8 kλ, depending on position angle. The statistic U was also minimized in six overlapping azimuthal sectors in the *u-v* plane to check for evidence of asymmetric expansion.

A bulk expansion age, $T_{\rm bulk}$, can be obtained from the best-fit *u-v* cell-size scaling between 1985 and 1990. Let f be the best-fit fractional contraction per year:

$$f = \frac{F}{t_0} , \quad (4)$$

where F is the full contraction measured over a time interval t_0. Then

$$T_{\rm bulk} = \frac{R}{V} = \frac{R}{fR} = \frac{t_0}{F} . \quad (5)$$

As the visibilities in the relevant portion of the *u-v* plane have been collected in different array configurations on different dates, t_0 is best estimated from a sum of configuration dates within the epoch (listed in Table 1), weighted by the number of visibilities between 0.8 and 3 kλ obtained in each configuration. The appropriate time baseline in this study is then 5.2 ± 0.1 yr.

Table 6 lists the scalings measured in various azimuthal sectors of the *u-v* plane, and the associated expansion timescales. As information in the *u-v* plane is unique over only 180° in position angle, these values really refer to averages between two opposing sectors within the remnant (e.g., 0°–60° *and* 180°–240° in position angle). Note that because we have not performed a careful absolute calibration between epochs, $S_{\rm bulk}$ does not give a reliable estimate of the secular brightness change in the bulk radio ring.

It appears that the bulk expansion of Cas A varies appreciably with position angle. Expansion ages of 750 yr (north-south) and 1300 yr (east-west) are obtained for the bulk motion of the radio plasma. These measurements are more in agreement with the results of Tuffs (1986) than those of Green (1988). *It is clear from our results that a significant deceleration of the bulk radio-emitting material in Cas A has already occurred.*

6. SUMMARY OF OBSERVATIONAL FINDINGS

We summarize here, for future reference, the major correlations between proper motion- and brightness-related quantities identified in previous sections for both compact and large-scale radio emission features in Cas A:

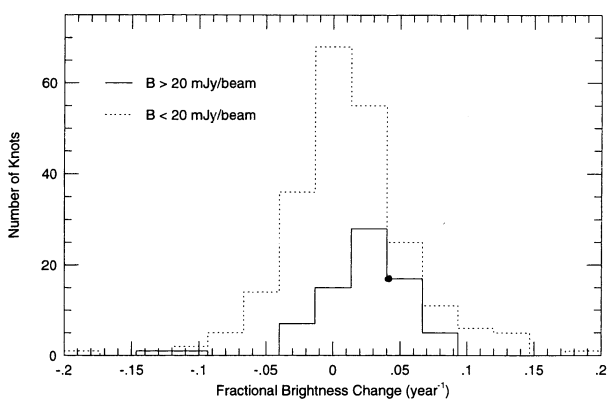

FIG. 15.—Histograms of annual fractional brightness change for knots brighter and fainter than 20 mJy beam^{-1}.

TABLE 6

SECULAR CHANGES IN THE VISIBILITY PLANE

UV P.A.	F (%)	$S_{\rm bulk}$	$T_{\rm bulk}$ (yr)
All	0.70 ± 0.05	1.114 ± 0.002	750 ± 60
0°–60°	0.70 ± 0.05	1.108 ± 0.004	750 ± 60
30°–90°	0.50 ± 0.05	1.098 ± 0.002	1000 ± 100
60°–120°	0.45 ± 0.05	1.118 ± 0.002	1300 ± 170
90°–150°	0.65 ± 0.05	1.118 ± 0.002	800 ± 70
120°–180°	0.70 ± 0.05	1.118 ± 0.002	750 ± 60
0°–30°, 150°–180°	0.65 ± 0.05	1.122 ± 0.002	800 ± 70

NOTES.—Best-fit contractions and brightness scaling factors computed for comparisons between the 1985 and 1990 *u-v* data at λ = 20 cm. Col. (1): Range in position angle in the *u-v* plane used in the comparison. Angles correspond to positional orientations of fringes in the map plane, measured from north through east. Col. (2): Best-fit baseline contraction factor. Col. (3): Best-fit visibility amplitude scaling factor $S_{\rm bulk}$. Col. (4): Bulk expansion timescale in sector.

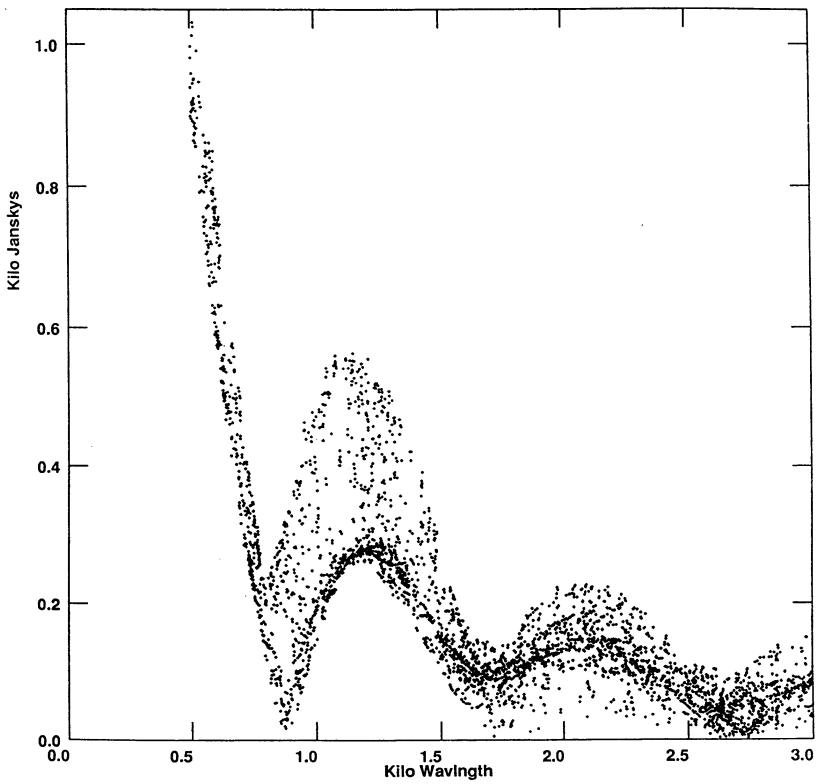

FIG. 16.—Visibility amplitudes on baselines between 0.5 and 3 kλ, plotted as a function of baseline for epoch 1985, $\lambda = 20$ cm

6.1. *Expansion Timescales*

1. The radio expansion center defined by our sample of knots is $\alpha(1950) = 23^h21^m10^s.3 \pm 0^s.2$, $\delta(1950) = +58°32'25''.6 \pm 3''.1$.

2. The characteristic timescale of expansion for compact features in the bright radio ring in Cas A is $\sim$950 yr. Outside the ring, timescales of 900–550 yr are found. Expansion timescale is inversely correlated with distance from the expansion center.

3. When the remnant is divided into azimuthal sectors, the expansion ages for compact features vary between $\sim$500 yr (in the east) and 2000 yr (in the west).

4. The longer timescales measured in the western and southwestern sectors of the remnant are primarily due to bright knots (faint knots show more consistent timescales around the remnant). Characteristic timescales of expansion are $\sim$900 and 750 yr for bright and faint knot populations, respectively.

5. The bulk expansion age of the large-scale radio-emitting material in Cas A varies between $\sim$750 yr (north-south) and 1300 yr (east-west).

6. Residuals to a linear expansion model show a considerable degree of nonradial motion in the western sector.

7. Although compact radio features in Cas A have been significantly decelerated since ejection, we do not find convincing evidence for a net radial deceleration of radio knots occurring over the 12 yr time period encompassed by this study.

8. The system of radio knots in Cas A do, however, appear to be undergoing a small, net northward-directed acceleration.

6.2. *Brightness Changes*

1. Relative to the large-scale emission in the remnant, compact features are found to be brightening at a mean rate of $\sim 1.6\%$ year^{-1}.

2. The most rapid fractional brightness changes occur among compact features in the southwest quadrant of the remnant and in the jet region.

3. The rate of fractional brightness change increases with distance from the expansion center for knots exterior to the radio ring. Knots inside the ring show a mean zero brightness change.

4. There is a small direct correlation between fractional brightness change and knot brightness for *bright* knots (no correlation exists among faint knots).

7. A DECELERATION-POWERED EMISSION MODEL FOR EJECTA COMPONENTS IN CASSIOPEIA A

We now synthesize the dynamical data discussed above and construct a model for the powering of radio emission features in Cas A on both small and large spatial scales. We will build on the following hypothesis: that the bulk of the emission processes operative in Cas A are primarily deceleration-powered. In other words, ejecta components begin to radiate only after enduring sufficient interaction with the surrounding medium. This is not an entirely new concept. As was stated above, deceleration is believed to play a primary role in powering both the bulk X-ray and radio shells in the remnant. The optical emission from FMKs is attributed to internal shocks generated in a collision between dense ejected clumps and the decelerated ejecta shell (Bell 1977). We contribute to this picture a new interpretation of the radiative evolution of compact radio features in Cas A.

As a paradigm for the early distribution of ejecta in Cas A, we draw on the supernova explosion model for a 15 $M_\odot$ star used by Jones, Smith, & Straka (1981, as adapted from Weaver, Zimmerman, & Woosley 1978). In this model, a diffuse exo-atmospheric skin of material between the stellar envelope and

the circumstellar medium is ejected homologously at high velocity. Upon passage of the blast wave, the interface between the mantle and the stellar envelope becomes Rayleigh-Taylor unstable—Jones et al. speculate that R-T fingers may decouple from the surrounding flow at this time and be ejected in clumpy form at a velocity somewhat lower than that of the diffuse material. The subsequent evolution of clumpy SNRs, subject to certain constraints guaranteeing self-similarity, was studied by Hamilton (1985). In Hamilton's models, ejecta clumps travel to a certain density-dependent distance before ablating away completely and melding with the diffuse ejecta.

In this section we outline the sequence of emission events from the different ejecta components in Cas A. In that the rate of deceleration of a given ejecta component of density ρ_c, moving in an ambient plasma of density ρ_{amb}, is related to its density contrast with the background medium, $\chi = \rho_c/\rho_{amb}$, it is expected that ejecta will "turn on" sequentially in order of increasing χ. We proceed in order of increasing internal density and therefore increasing deceleration timescale, emphasizing those components which give rise to nonthermal radio emission. A more detailed comparison of observations and numerical simulations of evolving clumpy ejecta is presented by AJRTK.

For the sake of this discussion, we will divide the system of ejecta in Cas A into two main components: the diffuse ejecta, and the clumpy ejecta. Clumpy ejecta will be further subdivided on the basis of density contrast with the surrounding medium. Those clumps with $\chi \gg 1$ will not yet have been significantly decelerated and will thus behave as semirigid bodies. Clumps with somewhat lower density contrast will be in the process of deceleration at the current epoch and are thus susceptible to deceleration-associated instabilities.

7.1. *Diffuse Ejecta*

The diffuse exoatmospheric material, ejected homologously at the highest velocities, rapidly sweeps up its own mass of ISM and thus decelerates first. The timescale for the deceleration of diffuse material will be on the order

$$t_{dec} \sim \frac{1}{v_{diff}} \left(\frac{3M_{diff}}{4\pi\rho_{amb}} \right)^{1/3}, \quad (6)$$

where M_{diff} is the mass of material ejected in diffuse form and v_{diff} is the average velocity with which this material was ejected. Estimates of the ambient density around Cas A have ranged between 0.2 cm^{-3} (Minkowski 1968, from H I observations) and 8 cm^{-3} (Peimbert 1971, from H II emission). We adopt here a value $n_{amb} = 2\ cm^{-3}$, which is consistent with densities obtained from a reverse shock model of the low-temperature X-ray ring (McKee 1974), and densities inferred from the current deceleration of the radio-emitting material (Gull 1973b; Braun 1987). The total mass of material ejected in diffuse form in the Cas A explosion is estimated by Braun (1987) to be 0.3 $M_\odot$. Assuming an ejection velocity of $\sim 10^4$ km s^{-1} (Braun 1987), a deceleration timescale of $t_{dec} \approx 110$ yr is obtained—significantly less than the current age of the remnant. This is consistent with our measurement of a significant bulk deceleration of the radio-emitting ejecta in Cas A, as presented in § 5. As tabulated in Table 6, expansion ages vary with position angle between 750 and 1300 yr ($v = 1800$ to 1200 km s^{-1}).

To maintain pressure equilibrium with the rarified shock-heated ISM behind the outer shock, or blastwave, the decelerated diffuse ejecta form a dense shell at the interface, as is demonstrated in the models of Gull (1973a). This decelerated surface is subject to Rayleigh-Taylor and Kelvin-Helmholtz instabilities which may serve to radially align and amplify any internal or swept-up magnetic fields. AR show that some type of early field amplification process is necessary to explain emissivities observed in compact features in the remnant.

As discussed by Bell (1977) and BGP, this contact surface is further disrupted when clumps of ejecta, ejected at lower initial velocities, catch up with the decelerated shell. These bullet-like clumps puncture the shell and leave expanding holes in its surface. As neighboring holes collide, material is compressed at the interfaces, giving rise to the honeycomb-like filamentary structures which are particularly evident in the spatially filtered image of Cas A in Figure 3. Material in these ridges will, with time, diffuse from the region of maximum compression, thus the sharpest and brightest filaments will be formed in the most violent or most recent collisions. The cellular patterns in Figure 3 are significantly brighter and better defined in the western hemisphere of the remnant than in the eastern hemisphere; Figure 12 shows that knots in western filaments are also brightening rapidly. This may reflect the fact that the ejecta shell is more decelerated in the west, thus enhancing the local velocity difference between shell and clumps. Some subset of the knots in our sample found at the radius of the radio ring is likely to be comprised of surface features associated with this decelerated shell.

7.2. *Clumpy Ejecta*

The behavior of a supersonic clump of gaseous ejecta moving into a medium of nonnegligible density is phenomenologically similar to the case of a cloud of material being overrun by a planar shock. The hydrodynamic evolution of shock-cloud interactions has frequently been the subject of numerical simulations, as this situation has bearing on the expansion of a supernova blastwave into an inhomogeneous medium (see, e.g., Woodward 1976; Nittman, Falle, & Gaskell 1982; Bedogni & Woodward 1990; Stone & Norman 1992). Models by Jones & Kang (1993) have included the first-order acceleration of particles and the back-reaction of cosmic-ray proton pressure on the various shocks which develop in the interaction. Most recently, Jones, Kang, & Tregillis (1994, hereafter JKT) have explored the plight of a gaseous projectile moving into a cold (unshocked) medium. They have generated a time sequence of synchrotron emissivity maps for clouds of various density contrasts which can be compared with evolving radio structures observed in Cas A (see AJRTK).

Several types of shocks develop in and around a supersonic clump of compressible material. A bow-shock forms in front of the clump to decelerate the incoming flow, and the stagnation pressure at the forward face of the clump drives a shock into its surface. This internal shock will traverse the clump on a timescale referred to by JKT as the "bullet-crushing" time, given by

$$t_{bc} \approx C(\chi) \frac{\chi^{1/2} D}{u_c}, \quad (7)$$

where u_c is the clump velocity, D is the clump diameter, and $C(\chi) < 1$. As the ambient material envelops the cloud, a series of tail-shocks develop behind the clump where the flow converges.

A given clump will begin to decelerate as soon as the internal shock reaches the back face of the cloud. JKT show that the

phase of ejecta clump deceleration is accompanied by a rapid turn-on in synchrotron emission, which is in many ways analogous to the radio turn-on predicted by Gull (1975) for decelerating diffuse ejecta. Magnetic fields are strongly amplified in the shear layers separating the cloud material from the ambient fluid. JKT find that the synchrotron emission from these boundaries strongly dominates the emission from particles compressed and accelerated by the bow shock. After $\approx 4t_{bc}$, the cloud is completely destroyed by Rayleigh-Taylor instabilities which develop at the forward face and ultimately reduce the cloud to filamentary shreds (Klein, McKee, & Colella 1990; Stone & Norman 1992).

The clumpy ejecta in Cas A are likely to be distributed over a wide variety of sizes and internal densities, and thus currently there must exist ejecta in many different stages of deceleration. Below we present observational evidence that suggests that clumpy ejecta in Cas A are indeed observed in both strongly and weakly decelerated states.

7.2.1. *Strongly Decelerated Clumps—the Bright Radio Knots*

The least dense clumps ejected in the explosion may have been stopped at the decelerated shell—others may have penetrated further before ablating and may now contribute to the diffuse plateau. The models of JKT predict that synchrotron turn-on occurs on timescales commensurate with the growth of large amplitude Rayleigh-Taylor instabilities, on the order of $3t_{bc}$.

This timescale can be used to estimate the density contrast of radio knots just turning on at the current epoch. We assume that clumps currently visible in the radio have initial ejection velocities bounded below by the velocity of the vast majority of undecelerated optical knots (~ 5000 km s^{-1}; RHFW) and above by the ejection velocity of the diffuse material ($\sim 10{,}000$ km s^{-1}; Braun 1987). Significant evolution occurs only after the clump collides with the decelerated shell, so this event marks $t = 0$ with respect to the turn-on timescale. If the shell has been expanding at ~ 1500 km s^{-1} since it decelerated, knots ejected with, e.g., $u_c = 7000$ km s^{-1} reached the shell 130 yr ago. Of these, the knots with $\chi = 20$ will have $3t_{bc} = 130$ yr. BGP have estimated a typical density of 30 cm^{-3} for several of their identified features, while estimates of the density of thermal material in the remnant needed to produce the observed Faraday rotation range between 2 cm^{-3} (Downs & Thompson 1972) and 8 cm^{-3} (Rosenberg 1970), so a density constrast on the order of 20 is not unreasonable. Knots of similar χ ejected with higher velocities will be in a more advanced stage of evolution.

Following the onset of deceleration, synchrotron emissivity in the models of JKT increases rapidly, with an e-folding timescale of $\sim \frac{1}{2}t_{bc}$. For the clumps described above, a brightening timescale of 20 years is predicted, in agreement with the distribution of knot lifetimes displayed in Figure 13. The model estimate, however, carries some uncertainty in that betatron and second-order acceleration have not been considered, and the clouds are highly idealized. While the simulations of JKT have not yet been carried through the entire radiative lifetime of a cloud, it is expected that synchrotron emissivity will continue to increase until the cloud is torn apart by the instabilities and dispersed.

Viewing the multiple epochs of images in time sequence, we find compact features in Cas A which have evolved in a manner very similar to that predicted by the models of JKT. Two such examples are provided in AJRTK. These knots turn on, brighten rapidly and are quickly destroyed through fragmentation.

A model of deceleration-induced radio brightening is consistent with the kinematic data presented above. In § 4 it was demonstrated that the expansion timescales of the brightest knots are, on average, longer than those of other compact features. This correlation is strongest for knots found outside the radio ring—a subset uncontaminated by surface features associated with the diffuse shell.

The weak yet significant positive correlation between knot brightness and rate of brightening suggests a convex brightening curve similar to that predicted by the models of JKT. The fact that the distribution of fractional brightness change peaks in the brightening regime indicates that knots do not in general suffer a lingering fading phase. They brighten, then burn out rapidly, in agreement with simulations (JKT).

7.2.2. *Weakly Decelerated Clumps: the Bow Shocks*

If a clump of ejecta has $\chi \gg 1$, it is dense enough to be considered a semirigid body in the context of the surrounding medium. A clump with high-density contrast will behave for some time period like a bullet, driving a bow shock into the ambient material and thereby compressing fields and accelerating particles. According to JKT, the clump itself remains virtually invisible in the radio until it has decelerated by $\sim 25\%$ (for $\chi = 30$). However, if viewed against a background of low emissivity, it may be possible to detect weak emission from particles and fields compressed by bow shocks. The faint paraboloidal structures seen around the edges of the Cas A remnant may indeed be bow shocks driven by moderately dense clumps of ejecta, as was proposed by BGP. The brighter, interior features identified by BGP are more likely to be associated with the decelerated ejecta clumps themselves because of their higher surface brightnesses.

The opening angle of a bow-shock should be concordant with its observed proper motion. BGP estimate the opening half-angles, μ, for their features to be between 12° and 32°, corresponding to a range in Mach number [given by $M = 1/\arcsin(\mu)$] of ~ 2–6 (these values are somewhat uncertain, however, due to necessary assumptions concerning projection angle). Reasonable agreement between these Mach numbers and observed proper motions can be obtained only if the clumps driving the bow shocks are assumed to be traveling in the post-blastwave fluid—the sound speeds expected in the unshocked circumstellar medium would yield Mach numbers on the order of 200.

The Mach number associated with a clump moving at a velocity v_c behind the blastwave of velocity v_s in a postshock medium with sound speed c_{ps} and velocity v_{ps} with respect to the outer shock is given by

$$M = \frac{[(v_c - v_s - v_{ps})]}{c_{ps}}, \tag{8}$$

where in the strong shock limit ($M \gg 1$)

$$c_{ps}^2 = 2\gamma v_s^2 \frac{(\gamma - 1)}{(\gamma + 1)^2}$$

$$v_{ps} = \frac{(\gamma - 1)}{(\gamma + 1)} v_s . \tag{9}$$

Equations (8) and (9) yield the expressions

$$M = \frac{(v_c - \frac{3}{4}v_s)}{v_s/1.26}\left(\gamma = \frac{5}{3}\right),$$

$$M = \frac{(v_c - \frac{6}{7}v_s)}{v_s/2.47}\left(\gamma = \frac{4}{3}\right). \quad (10)$$

As an example, the blast-wave velocity needed to produce a Mach number of 2.3 (as inferred from the shock opening angle) for knot 291 (BGP's bow shock C), given the observed proper motion of $v_c \sim 4300$ km s^{-1}, is $v_s \sim 1670$ km s^{-1} for $\gamma = 5/3$. This is consistent with the blast-wave velocity which can be inferred (given certain assumptions) from the high-temperature X-ray emission found beyond the soft X-ray shell (Fabian et al. 1980).

True bow shocks can also be distinguished from other emission features by a characteristic signature in polarization. Numerical simulations of astrophysical bow shocks (Coleman & Bicknell 1985) have shown that swept-up ambient field lines will become aligned tangential to the shock front. Disrupting clumps of ejecta and other types of vortical fluid motions, however, will also perturb the local magnetic field, thus a deviant polarization angle is not itself an unambiguous bow-shock identifier.

Additional bow-shocks have been identified in maps of polarized intensity at 1.4 GHz (AKR). The polarized signal that survives Faraday depolarization at this frequency defines a set of crescent-shaped structures which lie outside the total intensity ring. We propose that these features delineate bow shocks driven by clumps of ejecta which have just emerged from a relatively high-density thermal X-ray environment. An examination of the polarization structure in the two best-defined arcs in the east shows that the fields in these features are indeed tangential (see AKR). These features are quite faint in total intensity—we are able to identify them only because the strong Faraday depolarization from the thermal shell has eradicated surrounding polarized emission.

In addition to the bow shocks, faint knots outside the radio ring are also probably associated with higher density clumps. These knots are distinguished from other compact radio features by their short expansion timescales. They are presumably excited by ejecta clumps dense enough to have suffered little interaction with the ambient medium to date. It may be that the faint knots in total intensity correspond to the apices of bow shocks driven by weakly decelerated clumps (see models of Coleman & Bicknell 1988); their associated paraboloidal sheaths, however, may be indiscernible in projection against the radio plateau.

7.2.3. *Weakly Decelerated Clumps: The Optical FMKs*

The optical line emission from the fastest moving compact features in Cas A has been modeled as arising from radiative shocks driven into dense clumps of ejecta upon impact with the decelerated ejecta shell. Preshock densities derived for FMKs range between 10–50 cm^{-3} (Contini 1987) and 165 cm^{-3} (Braun 1987). The lack of deceleration in the observed proper motions of FMKs also attests to high internal densities.

Clumps will remain optically active until the internal shock has traversed its length, thus the timescale for optical emission should be on the order of a bullet-crushing time. Kamper & van den Bergh (1976) measure characteristic optical knot e-folding lifetimes of 25 years. If we assume this brightness rise time corresponds roughly to the timescale for the internal shock to reach the core of the clump, then an optical lifetime of $\sim\frac{1}{2}t_{bc}$ is obtained. van den Bergh (1971) quotes a typical FMK diameter of 2″, so with $\chi \sim 100$ and $u_c = 6000$ km s^{-1}, optical knot lifetimes are expected to be $\sim$20 years—comparable to the observed lifetimes. These ejecta will also drive bow shocks, but because optical knots are observed primarily in the vicinity of the bright radio ring, the faint radio emission from these bow-shocks may be imperceptible at this time. JKT's models predict, however, that these knots will brighten rapidly in the radio on a timescale of order $3t_{bc} \sim 60$ yr, after they have decelerated by $\sim$25%.

7.3. *Summary of Model*

A deceleration-powered model for the emission processes active in Cas A is consistent with the kinematic data presented in § 4. These data are summarized graphically in Figure 17, where inverse timescales for the brightest and faintest radio knots and the FMKs have been plotted as a function of distance from the optical expansion center. Faint radio knots beyond the radio ring (at $\sim$100″) have preferentially shorter expansion timescales than bright knots—these are less decelerated, thus field-amplifying instabilities are in an earlier stage of development. The gap in expansion timescale between the fastest moving faint radio knots and the optical FMKs represents a period of relative invisibility which occurs after the internal shock has traversed the length of the cloud, but before the onset of dynamical instabilities. In this figure, we see that faint radio knots begin to appear after having been decelerated by $\sim$25%, as predicted by the models of JKT. This interpretation is subject to the following caveat: we do not suggest that all radio bright knots were once optical-emitting knots (clumps must exceed some minimum internal density to facilitate short timescale recombination behind the internal shock), but we do predict that all optical knots will become radio knots.

The azimuthal variations in the expansion age derived for radio knots indicate varying degrees of deceleration, and therefore varying amounts of power available for emission processes. This supposition finds support in a comparison of temperature variations in the X-ray ring and a measure of deceleration among compact radio features (Fig. 18). Fabian et al. (1980) have modeled the temperature of the soft X-ray emitting material in Cas A within annuli subdivided into six azimuthal sectors. Here we have plotted the temperature modeled for the annulus containing the peak X-ray intensity (measured with the *Einstein* HRI detector) in each sector against the fractional deceleration experienced by all radio knots within that sector (as given by the ratio of the expansion age to the true remnant age).[2] In the eastern part of the remnant, where the X-ray temperatures are lowest, we find the shortest expansion timescales. Material ejected in these directions has been less strongly decelerated, thus the local reverse shock is less well-developed. We see here in a very direct sense how the momentum lost by decelerated material is diverted into radiative processes. It must be noted, however, that the temperature determinations by Fabian et al. (1980) do not take into account spatially varying line-of-sight absorption across the remnant, as is implied by the H I optical depth measurements of Bieging, Goss & Wilcots (1991). The effects of variable absorption on the observed soft X-ray intensity distribution is described in

[2] In sector V, temperatures from the two adjacent annuli spanned by the X-ray ring have been averaged. Note that these sectors do not precisely coincide with those displayed in Fig. 8.

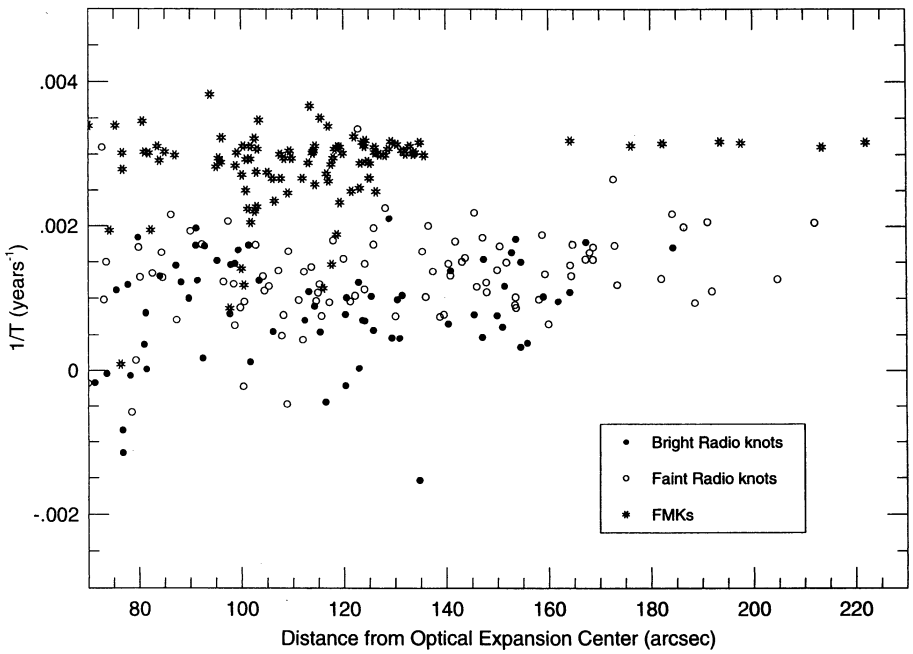

FIG. 17.—Inverse expansion timescales as a function of radius for bright and faint radio knots and FMKs (FMK proper motions have been taken from Kamper & van den Bergh 1976 and van den Bergh & Kamper 1983). Radio knots brighter than 20 mJy beam^{-1} and fainter than 10 mJy beam^{-1} have been plotted. Only knots at large radii, where expansion timescales are well determined, are displayed.

Keohane et al. 1995. There is also strong evidence of an asymmetry in the dynamics of the X-ray emitting gas (Markert et al. 1983; Holt et al. 1994). Detailed comparisons of radio, X-ray, and optical motions need to performed in the future with higher quality maps of X-ray temperatures and absolute calibration of the X-ray Doppler velocities.

8. CONCLUSIONS

It has been determined that the bulk of the radio-emitting material in Cas A has been significantly decelerated by the present epoch. Although the remnant is globally in a decelerating phase, it is apparent that a range of dynamical conditions apply to the various ejecta components in Cas A. Azimuthally varying degrees of deceleration are measured for the diffuse ejecta, while clumpy components are found in both freely expanding and strongly decelerated states. The current stage of deceleration of a given component is probably determined by its density contrast with the surrounding medium.

We have demonstrated how variable deceleration of ejected material translates into variable radio brightness. The deceleration-powering of radio emission applies both to large- and small-scale ejecta components. Under Gull's (1975) model, the radio turn-on of the ejecta shell in young supernova remnants occurs over relatively long timescales, thus it is unlikely

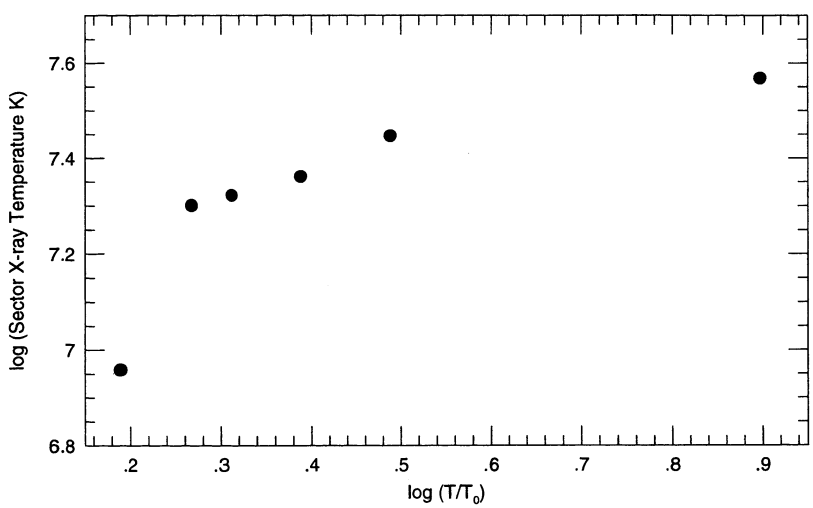

FIG. 18.—Temperatures in the X-ray ring, modeled in azimuthal sectors (from Fabian et al. 1980) vs. the fractional deceleration of compact radio features in corresponding sectors. Data are plotted on a log-log scale.

that the progression of this process can be observed directly. We now have direct evidence that Gull's mechanism for deceleration-induced magnetic field amplification is in fact plausible when applied to small clumps of ejecta, and that it is likely to be driving the rapid radio brightening observed among compact radio knots in Cas A.

The observations presented here suggest that there is a constant transfer of ejected material in Cas A from a clumpy to a diffuse state. Mass is transported invisibly at most wavelengths in clumpy form out to some maximum radius determined by the local density contrast, visible only briefly in optical emission upon collision with the decelerated ejecta shell. When the clump has interacted sufficiently with the surrounding material, it decelerates, brightens rapidly in the radio, and is destroyed through dynamical instabilities, thereby melding with the diffuse component.

This work was supported, in part, by the NSF through grants AST-8720285 and AST-9100486. We also appreciate the support of the Minnesota Supercomputer Institute for some of the computer processing. We are grateful for the extensive archive of Cambridge 5 km and VLA data from the late P. Angerhofer, and from R. Braun, S. Gull, R. Perley, and R. Tuffs. We also thank the referee, John Dickel, for questions and criticisms that led to significant improvements in this work. Discussions with Tom Jones and Hyesung Kang were especially helpful in formulating ideas about dynamical models of the remnant.

REFERENCES

Anderson, M. C. 1993, Ph.D. thesis, Univ. Minnesota
Anderson, M. C., Jones, T. W., Rudnick, L., Tregillis, I., & Kang, H. 1994, ApJ, 421, L31 (AJRTK)
Anderson, M. C., Keohane, J. W., & Rudnick, L. 1995, ApJ, 441, 300 (AKR)
Anderson, M. C., & Rudnick, L. 1995, in preparation (AR)
Anderson, M., Rudnick, L., Leppik, P., R., & Braun, R. 1991, ApJ, 373, 146
Ashworth, W. 1980, J. Hist. Astron., 11, 1
Avni, Y. 1976, ApJ, 210, 642
Baars, J. W. M., Genzel, R., Pauliny-Toth, I. I. K., & Witzel, A. 1977, A&A, 61, 99
Bedogni, R., & Woodward, P. R. 1990, A&A, 231, 481
Bell, A. R. 1977, MNRAS, 179, 573
Bell, A. R., Gull, S. F., & Kenderdine, S. 1975, Nature, 257, 463
Bieging, J. H., Goss, W. M., & Wilcots, E. M. 1991, ApJ, 75, 999
Braun, R. 1987, A&A, 171, 233
Braun, R., Gull, S. F., & Perley, R. A. 1987, Nature, 327, 395 (BGP)
Coleman, C. S., & Bicknell, G. V. 1985, MNRAS, 214, 337
———. 1988, MNRAS, 230, 497
Contini, M. 1987, A&A, 183, 53
Dickel, J. R., & Greisen, E. W. 1979, A&A, 75, 44
Downs, G. S., & Thompson, A. R. 1972, AJ, 77, 120
Fabian, A. C., Willingale, R., Pye, J. P., Murray, S. S., & Fabbiano, G. 1980, MNRAS, 193, 175
Fesen, R. A., Becker, R. H., & Goodrich, R. W. 1988, ApJ, 329, L89
Green, D. A. 1988, in Supernova Remnants and the Interstellar Medium, ed. R. S. Roger & T. L. Landecker (Cambridge: Cambridge Univ. Press), 205
Gull, S. F. 1973a, MNRAS, 161, 47
———. 1973b, MNRAS, 162, 135
———. 1975, MNRAS, 171, 263
Hamilton, A. J. S. 1985, ApJ, 291, 523
Holt, S. S., Gotthelf, E. V., Tsunemi, H., & Negoro, H. 1994, PASJ, 46, L151
Jones, T. W., & Kang, H. 1993, ApJ, 402, 560
Jones, T. W., Kang, H., & Tregillis, I. 1994, ApJ, 432, 194 (JKT)
Jones, E. M., Smith, B. W., & Straka, W. C. 1981, ApJ, 249, 185
Kamper, K., & van den Bergh, S. 1976, ApJS, 32, 351
Keohane, J. W., Rudnick, L., & Anderson, M. C. 1995, in preparation
Klein, R. I., McKee, C. F., & Colella, P. 1990, in Evolution of the Interstellar Medium, ed. L. Blitz (Berkeley: ASP), 117
McKee, C. F. 1974, ApJ, 188, 335
Markert, T. H., Canizares, C. R., Clark, G. W., & Winkler, P. F. 1983, ApJ, 268, 134
Minkowski, R. 1968, in Stars and Stellar Systems, Vol. 7, ed. B. M. Middlehurst & L. H. Aller (Chicago: Univ. of Chicago Press), 623
Napier, P. J., Thompson, A. R., & Ekers, R. D. 1983, Proc. IEEE, 71, 1295
Nittman, J., Falle, S. A. E. G., & Gaskell, P. H. 1982, MNRAS, 201, 833
Peimbert, M. 1971, 170, 261
Press, W. H., Teukolsky, S. A., Vetterling, W. T., & Flannery, B. P. 1992, in Numerical Recipes in Fortran (Cambridge: Cambridge Univ. Press), 634
Reed, J. E., Hester, J. J., Fabian, A. C., & Winkler, P. F. 1994, preprint (RHFW)
Rosenberg, I. 1970, MNRAS, 151, 109
Stone, J. M., & Norman, M. L. 1992, ApJ, 390, L17
Tuffs, R. J. 1983, in Proc. IAU Symp. 101, Supernova Remnants and Their X-Ray Emission, ed. J. Danziger & P. Gorenstein (Dordrecht: Reidel), 49
———. 1986, MNRAS, 219, 13
van den Bergh, S. 1971, ApJ, 165, 457
van den Bergh, S., & Kamper, K. W. 1983, ApJ, 268, 129
van Vleck, J. H., & Middleton, D. 1966, Proc. IEEE, 54, 2
Weaver, T. A., Zimmerman, G. B., & Woosley, S. E. 1978, ApJ, 225, 1021
Woodward, P. R. 1976, ApJ, 207, 484